Data-Driven Modal Analysis of Turbulent Momentum Exchange and Heat Transfer in Composite Porous Fluid Systems

Data-Driven Modal Analysis of Turbulent Momentum Exchange and Heat Transfer in Composite Porous Fluid Systems

Mohammad Jadidi*, Yasser Mahmoudi
School of Engineering, The University of Manchester, M13 9PL, Manchester, UK
*Corresponding author: mohammad.jadidi@manchester.ac.uk

Abstracts

This paper investigates the dynamics governing turbulent momentum exchange and heat transfer between pore flow within porous media and the turbulent flow passing over it. Employing high-fidelity pore-scale large eddy simulation, our investigation explores the fundamental mechanisms driving these phenomena. Modal analysis based on snapshot Proper Orthogonal Decomposition (POD) is employed to quantify the modes of interaction between porous and non-porous regions, providing a comprehensive understanding of the underlying processes. Spatial and temporal modes reveal the existence of localized flow structures at the pore scale, contributing to time-varying patterns of information exchange. At the commencement of the porous block, the mean flow (Mode = 0) from the porous to the non-porous region is the dominant mechanism in momentum exchange and heat transfer. This mode facilitates convective heat transfer from the porous to the non-porous region through upward and forward flow movements, showcasing positive flow leakage. In addition to the mean flow, the turbulent flux inherent in alternate POD modes (Mode ≠ 0) plays a substantial role in information propagation, influencing diverse directions. Spatial modes, complemented by statistical analysis, uncover a significant likelihood of observing negative vertical velocity values in the wake of the porous ligaments at the porous-fluid interface, indicative of negative flow leakage. This negative flow leakage precisely corresponds to the local penetration of fluid from the non-porous region into the porous region. Furthermore, our study reveals that information exchange via turbulence fluctuations manifests through complex outward and inward interactions in regions characterized by substantial positive flow leakage. Notably, these regions exhibit a distinct tendency for high-momentum streamwise-oriented flow to migrate outward from the porous region into the non-porous region (outward interactions). Conversely, inward interactions arise in these regions when the instantaneous magnitude of positive flow leakage is smaller than the mean value of positive flow leakage, emphasizing the pulsating nature of positive flow leakage. Finally, the distribution of the Nusselt number highlights that more than 60% of total heat transfer occurs within the initial one-third of the porous block length. Significantly, a notable portion of the porous ligaments experiences insufficient cooling due to positive flow leakage, underlining the critical implications of these findings for the understanding of turbulent momentum exchange and heat transfer in a composite porous-fluid system.

Keywords: Porous media; Turbulent flow; Modal analysis; Momentum exchange; Heat transfer; Flow leakage; Stochastic metal foam.

Nomenclature

variable	Meaning	Unit
d	Mean porous ligament diameter	m
f	Frequency	1/s
f_s	Sampling frequency for modal analysis	1/s
h	Height of the porous block	m
h_c	Convective heat transfer coefficient	W/m^2.K
H	Channel height	m
k	Turbulent kinetic energy	m^2/s^2
k_f	Thermal conductivity of the working fluid	W/m.K
L	Length of the porous block	m
Q_{in}^{Porous}	Flow rate that enters the porous block from the frontal face	m^3/s
Q_{lx}^{Porous}	Flow rate that leaks from the x-percentage of the porous-fluid interface	m^3/s
$Re_h = U_{in}h/\upsilon$	Reynolds number based on the inlet bulk velocity and channel height	–
$Re_d = U_{in}d/\upsilon$	Reynolds number based on the inlet bulk velocity and ligament diameter	–
$St = fh/U_{in}$	Strouhal numbers based on the height of the porous block	–
$St_d = fd\varepsilon/U_{in}$	Strouhal numbers based on the mean porous ligament diameter	–
t	Time	s
$t^* = t \times U_{in}/h$	Non-dimensional time unit	–
T	Temperature	K
T'	Temperature fluctuation, $T' = \bar{T} - \langle\bar{T}\rangle$	K
$\overline{\mathbb{T}} = \frac{T}{T_{s-T_{in}}}$;	Non-dimensional temperature	–
Δt	Time step	s
u	Streamwise velocity component	m/s
u_i'	Velocity fluctuation in ith direction, $u_i' = \bar{u}_\iota - \langle\bar{u}_\iota\rangle$	m/s
$u_i^{*\prime} = u_i'/U_{in}$	Non-dimensional velocity fluctuation in ith direction	–
U_{in}	Inlet bulk velocity	m/s
v	Vertical velocity component	m/s
x	Streamwise direction	m
y	Vertical direction	m
z	Spanwise (Lateral) direction	m
Symbol		
Υ	Pearson linear correlation coefficient	–
ε	Porosity	–
σ^r	The r^{th} eigenvalue corresponds to the r^{th} POD mode	–
$\sigma_u = u'/u_{RMS}$	Non-dimensional streamwise velocity fluctuation	–
$\sigma_v = v'/v_{RMS}$	Non-dimensional vertical velocity fluctuation	–
τ_{ij}	Sub-grid scale (SGS) turbulent stress tensor	m^2/s^2
υ	Molecular kinematic viscosity	m^2/s
υ_{SGS}	Sub-grid scale eddy viscosity	m^2/s
$\psi^r(t)$	rth temporal modes in POD analysis	m^2/s
$\phi_i^r(\vec{x})$	ith compound of the rth spatial mode in POD analysis	–
φ_u	Streamwise component of POD mode	–
φ_v	Vertical component of POD mode	–
Δ	Filter width	m
$\Theta = \frac{T - T_{inlet}}{T_{wall} - T_{inlet}}$	Non-dimensional temperature	–
$\theta = \frac{T'}{T_{wall} - T_{inlet}}$	Non-dimensional temperature fluctuation	–
$\overrightarrow{\quad}$	Vector with three components in x, y and z directions	–
$\overline{\quad}$	Filtration (top hat filter)	

$\langle\ \rangle$	Time-averaging operator	–
Subscript		
in	Inlet	–
res	Resolved by LES	–
RMS	Root mean square	–
s	Surface of pore element	–
SGS	Sub-grid scale	–
Superscript		
$'$	Fluctuation	–
r	r^{th} POD mode	–
Abbreviation		
$BR = h/H$	Blockage ratio, i.e., ratio of the porous block's height to channel height	–
CFL	Courant–Friedrichs–Lewy number	–
JPDF	Joint probability density function	–
LES	Large Eddy Simulations	–
Nu	Nusselt number	–
POD	Proper Orthogonal Decomposition	
TKE	Turbulent kinetic energy	m^2/s^2

1 Introduction

Understanding turbulent momentum exchange and heat/mass transfer in porous media with stochastic pore distribution has found extensive applications in various man-made and natural contexts. These applications include heat transfer devices for electronic equipment heat dissipation [1-3], batteries and energy storage [4-6], and phase change heat transfer [7-9]. Additionally, the fundamental physics governing natural phenomena, such as flow over vegetation [10, 11], can be modelled by incorporating the concept of porous materials with stochastic pore distribution.

For studying momentum exchange and heat/mass transfer between porous and non-porous regions, a composite porous-fluid system serves as a representative model [12]. The flow physics within these systems pose considerable complexity. **Figure 1** provides a schematic representation, illustrating key vortical structures and flow phenomena in different regions of the composite porous-fluid system. The figure depicts the boundary separation at the leading edge of the porous block, the formation of reverse flow preceding this edge, and the separation and reattachment of the boundary layer on the top porous-fluid interface between porous and non-porous regions. Additionally, flow separation after the trailing edge of the porous block leads to wake formation. Various configurations for representing porous media, such as spheres, rods, stochastic metal foam, or latex structures, are possible. In this paper, the porous media are modelled using stochastic metal foam.

In composite porous-fluid systems, the presence of a porous-fluid interface between porous and non-porous

regions introduces a complex interplay of fluid dynamics that significantly influences transport phenomena. This interface acts as a boundary where the porous medium, characterized by its interconnected network of void spaces, meets a non-porous region. The transition between these distinct regions leads to intriguing phenomena, impacting fluid flow, heat transfer, and mass transport. The porous-fluid interface governs the exchange of momentum and energy, making it a critical zone for studying the interactions between the porous and non-porous regions.

Despite the evident relevance and significance of turbulent flow and heat/mass transfer in such a system, a comprehensive explanation faces challenges. The primary obstacle lies in the inherent complexities associated with in-situ measurements of flow properties and thermal characteristics within the confined and intricate flow passages dictated by stochastic pore distribution. This limitation hinders a comprehensive understanding of turbulent momentum exchange and heat/mass transfer within these systems.

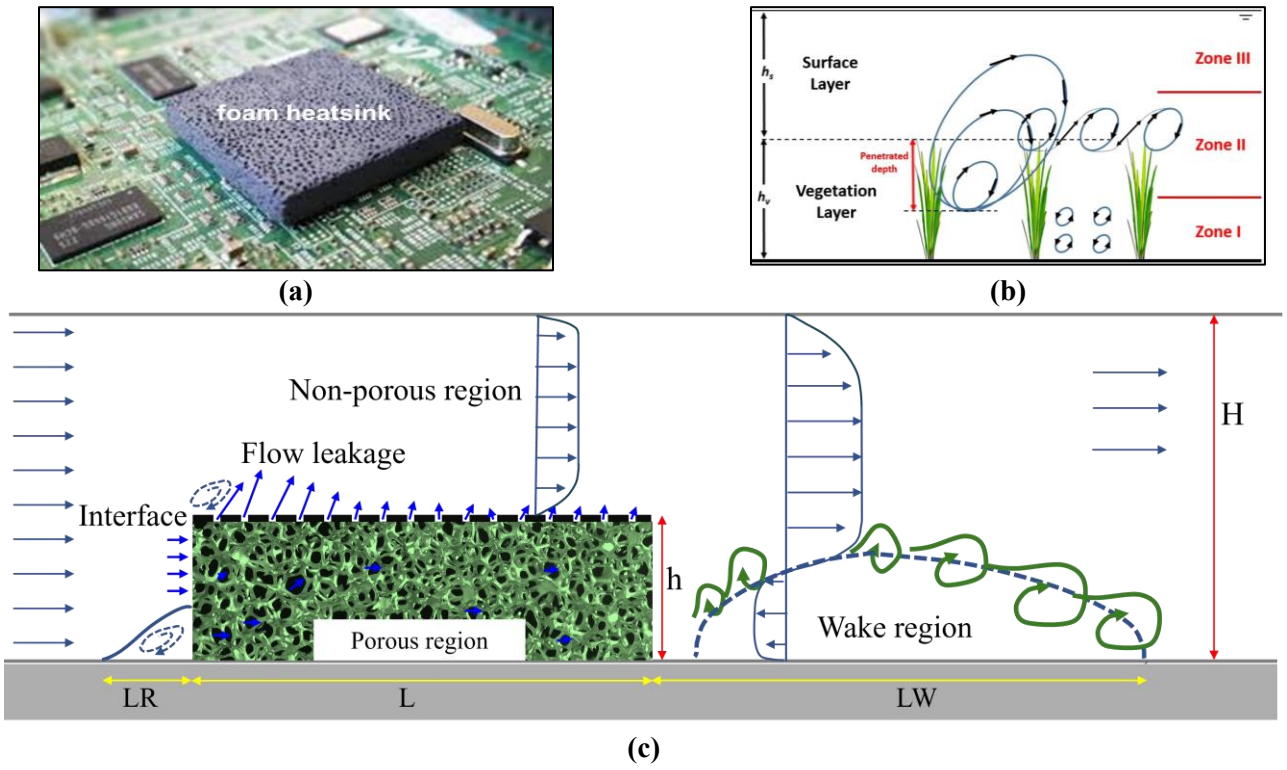

Figure 1. A composite porous-fluid system is employed as a representative model to investigate momentum exchange and heat/mass transfer dynamics between porous and non-porous regions. **(a)** Foam heat sink utilized in cooling techniques: A man-made composite porous-fluid system [13]; **(b)** Channel flow covered by vegetation: A natural composite porous-fluid system [10]; **(c)** Schematic depiction highlighting the intricate flow physics and vortical structures across distinct zones within a composite porous-fluid system.

The pore-scale analysis is currently providing novel insights into the flow dynamics and transport

phenomena in composite porous-fluid systems [14-18]. Quadrant analysis reveals that the exchange of information between porous and non-porous regions involves mechanisms characterized by “injection” and “suction” events [16, 19, 20]. The permeable porous-fluid interface facilitates the identification of injection events, signifying the flow from the pore space to the non-porous flow, and suction events, denoting the flow from the non-porous flow into the pore space. The occurrence of ejection events ($v' < 0$, where v' is the wall-normal velocity fluctuation) is statistically correlated with the simultaneous presence of large-scale regions of $u' > 0$ (where u' denotes the streamwise velocity fluctuation in the non-porous flow), and vice versa [17, 21, 22]. This negative correlation between u' and v' leads to the generation of strong ejection and sweep events, as indicated by $u'v' < 0$.

Experimental measurements in a flow adjacent to a porous layer provide significant insights [16, 21, 23]. The measurements show the presence of a shear layer with regular vortex structures over the porous block, evolving downstream to attain equilibrium width and vortex size [23]. The vortex structure exhibits robust crossflows, featuring sweeps from the non-porous region and ejections from the porous region. These dynamics result in momentum and mass fluxes across the interface, with the sweeps playing a crucial role in sustaining coherent structures by amplifying shear and energy production at the interface.

There is an intense transport of turbulent kinetic energy (TKE) from the surface to the subsurface flow, as reported in [24]. Evidence shows that the transport of TKE toward the lower bed levels is primarily driven by pressure fluctuations. Another study [25], has shown that the local pressure gradients are the primary mechanism for energy transfer from the freestream flow to the subsurface flow. These findings validate the robust linkage between the porous and non-porous region and the vertical fluid transport across the permeable interface, initially reported in [17].

Furthermore, the evidence demonstrates an exponential decay of mean velocities and turbulence intensities within the permeable wall [22, 26]. This decay phenomenon has been observed in various experimental studies involving different porous configurations [27-29]. Pressure measurements conducted within natural sediment beds have revealed that around 90% of high-frequency fluctuations are damped at a depth in the bed equivalent to approximately 4.5 times the particle diameter [30]. Additionally, it has been revealed that high-frequency oscillations dissipate more rapidly than low-frequency oscillations, suggesting that permeable walls act as low-pass filters, selectively attenuating high-frequency fluctuations.

Momentum enhanced between porous and non-porous regions has been numerically investigated extensively. Results from Direct numerical simulations (DNS) [31] have shown that the porosity significantly impacts the fluid motion near the interface and, consequently, turbulence transportation. The turbulent kinetic energy budgets demonstrated that pressure transportation and turbulent diffusion play the role of energy source and sink, which provide the possibility of turbulence transportation from the clear fluid into the porous region. Pressure perturbations induced by the Kelvin-Helmholtz (K-H) instability over the porous layer show that the turbulent coherent structure is shredded over the porous layer and large-scale intermittent fluctuations are induced inside the porous layer [32]. Turbulent flow with passive scalar transport within a channel partially filled with an array of spherical particles shows that the large turbulence structures generated at the permeable layer-fluid interface penetrate the porous media, enhancing scalar transport from the channel wall [33].

Moreover, recent investigations into composite porous-fluid systems, such as those involving a finite porous block immersed in turbulent channel flow [14, 34, 35], have identified unique mechanisms for momentum and energy exchange across the porous-fluid interface. These observations stand in contrast to the dynamics discussed earlier in the context of fully-developed porous channel flow. It has been speculated that in these composite systems, information transfer (turbulent momentum exchange and heat transfer) between the porous and non-porous regions is primarily governed by the leakage of the flow from the porous region to the flow passing over it in the non-porous region [12, 36]. While the mechanisms of turbulent momentum exchange and heat transfer have been explored in these studies, the underlying dynamic physical mechanism of flow leakage and its influence on controlling the flow and turbulent properties of the flow in the porous and non-porous regions and characteristics of the turbulent boundary layer at the interface have not yet been understood. Additionally, the porous structure has been modelled using a cubic packed arrangement formed from spheres.

The preceding review highlights a substantial gap in our understanding of turbulent momentum exchange and heat transfer within composite porous-fluid systems. Previous investigations have exposed divergent transport phenomena when considering a finite porous block in turbulent channel flow versus fully developed channel flow. Moreover, the majority of past research has focused on porous structures with simplified geometries, such as smoothed and disjointed cubes or spheres. This narrow focus has created a distinct deficiency in our fundamental comprehension, particularly for porous media distinguished by stochastic pore distribution, leaving a critical void in the current state of knowledge.

Therefore, investigating at the pore scale is essential to elucidate the complexities of turbulent momentum exchange and heat transfer across the porous-fluid interface in composite porous-fluid systems with stochastic pore distribution. This study employs high-fidelity pore-scale Large Eddy Simulations (LES) of composite porous-fluid systems, varying Reynolds numbers and porosities. The primary objectives are twofold: (i) to develop a novel methodology utilizing data-driven modal analysis to quantify momentum exchange and heat transfer dynamics between porous and non-porous regions; and (ii) to explore the respective contributions of mean flow and turbulence fluctuations to momentum exchange and heat transfer. A pioneering application of data-driven modal analysis, incorporating Proper Orthogonal Decomposition (POD) and time–frequency analysis, is introduced for the first time in the porous flow community to assess the time-dependent interaction of dominant flow structures in porous and non-porous regions. Furthermore, the discussion delves into the roles of convective and turbulent fluxes arising from mean and turbulence fluctuations, shedding light on their combined impact on overall heat transfer between the porous and the non-porous regions. Notably, this study pioneers the use of modal analysis to quantify the influence of convective and turbulent fluxes stemming from mean and turbulence fluctuations. Through this research, the time-dependent mechanisms governing information exchange between porous and non-porous regions in composite porous-fluid systems characterized by stochastic pore distribution are unveiled.

2 Computational methodology

2.1 Computational domain and boundary conditions

The computational geometry consists of a channel flow with dimensions of $30h$, $2h$, and $1.3h$ in the x, y, and z directions, respectively. "h" is the height of the porous block. A porous bluff body characterized by blockage ratio ($BR = h/H$) and aspect ratio ($AR = L/h$) of BR = 0.5 and AR = 3.33 is mounted inside the channel at x/h = 0, as shown in **Figure 2(a)**. Various configurations, such as spheres [14], rods [31], or latex structures [37] can be employed to represent porous media. In this study, stochastic metal foam is utilized for modeling the porous media; This choice enables a more detailed exploration of the intricate dynamics and interactions within the composite porous-fluid system, shedding light on the complex nature of momentum exchange and heat transfer in such systems. Two different stochastic metal foams with porosities, ε = 85% (low porosity) and ε = 91% (high porosity), are employed as shown in **Figure 2(b, c)**. The porosity of metal foams used in industry can vary depending on the specific application and desired properties. However, typical values of porosity for metal foams commonly used in industrial applications range from around 70% to 95%. Two Reynolds (Re_h) numbers, 1800 and 7200 based on the inlet velocity

(U_{in}) and the porous block height (h) are considered for each porosity. The corresponding Re_d numbers based on the inlet bulk velocity and mean porous ligament diameter (d) are 327 and 1310 for low-porosity cases and 203 and 812 for high-porosity cases. The applied boundary conditions are displayed in **Figure 2(a)**.

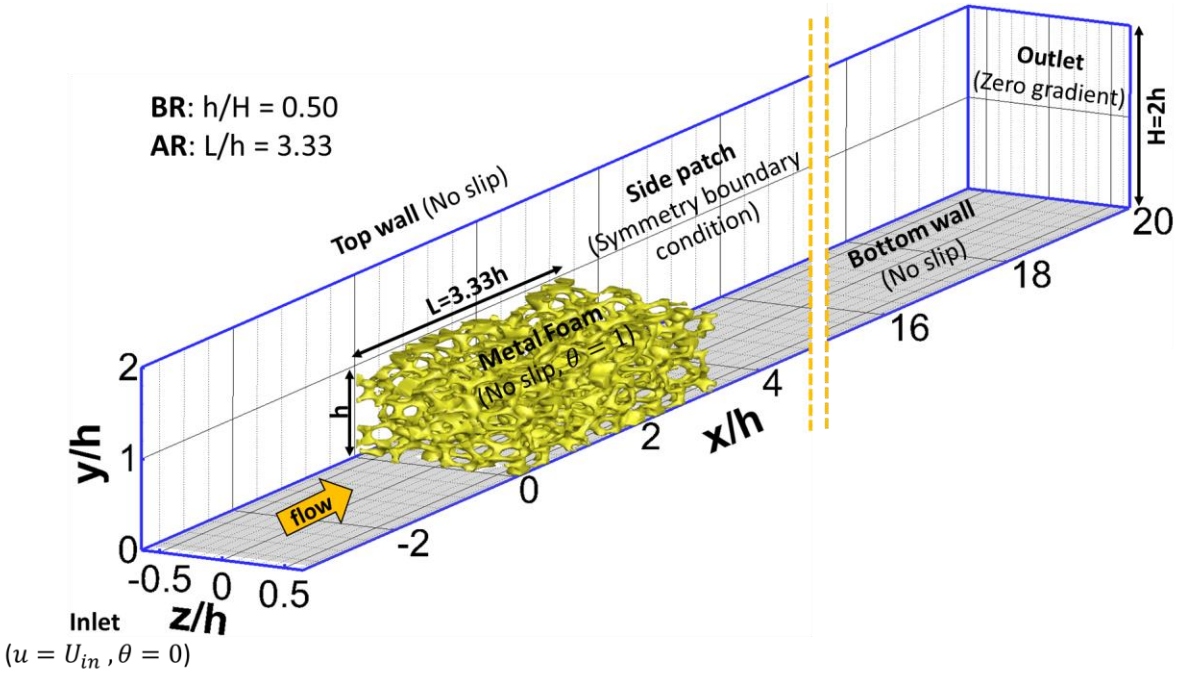

(a)

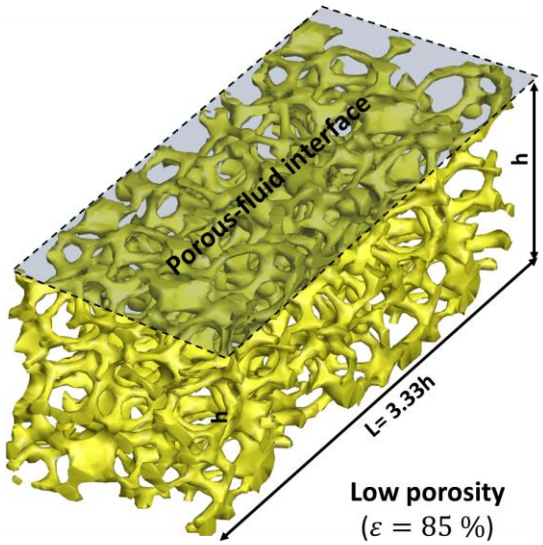

(b)

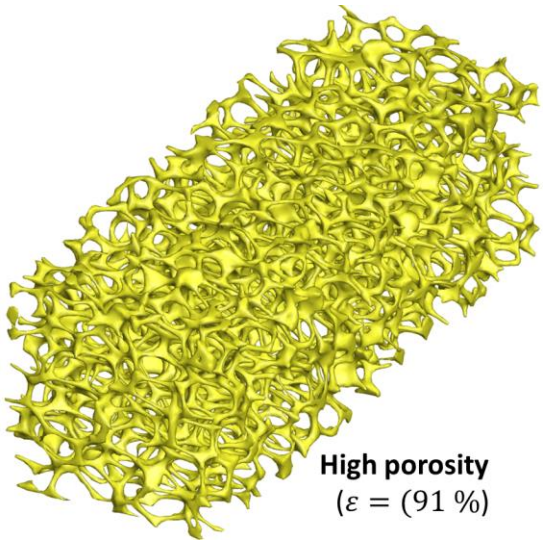

(c)

Figure 2. A composite porous-fluid system with stochastic metal foam porous block; **(a)** Computational domain and boundary conditions; **(b)** Low porosity (ε = 85%) porous block; **(c)** High porosity (ε = 91%) porous block.

2.2 Numerical details and validation

The governing equations for the incompressible flow in the present study are continuity, Navier-Stokes (momentum), and energy equations. Top-hat filtering is applied to the governing equations, resulting in the resolved LES equations as follows [38]:

$$\frac{\partial \overline{u_i}}{\partial x_i} = 0 \tag{1}$$

$$\frac{\partial \overline{u_i}}{\partial t} + \frac{\partial}{\partial x_j}\left(\overline{u_i}\,\overline{u_j}\right) = -\frac{1}{\rho}\frac{\partial \bar{p}}{\partial x_i} + \frac{\partial}{\partial x_j}\left(\upsilon \frac{\partial \overline{u_i}}{\partial x_j} - \tau_{ij}\right) \tag{2}$$

$$\frac{\partial \overline{\Theta}}{\partial t} + \frac{\partial}{\partial x_j}\left(\overline{\Theta}\,\overline{u_j}\right) = \frac{\partial}{\partial x_j}\left((\alpha + \alpha_{SGS})\frac{\partial \overline{\Theta}}{\partial x_j}\right) \tag{3}$$

Here, we use the symbol $(\overline{...})$ to denote the filtration operation. Accordingly, the filtered pressure, temperature, and velocity in the i^{th} direction are represented by $\overline{p}$, $\overline{\Theta}$ and $\overline{u_i}$, respectively. To estimate the sub-grid scale (SGS) stress (defined as $\tau_{ij} = \overline{u_i u_j} - \overline{u_i}\,\overline{u_j}$), we employ a localized dynamic k_{SGS}-equation model [39]. The governing filtered equations are discretized using the finite volume method within the open-source CFD package, OpenFOAM [40]. To solve the governing equations, we use the PISO algorithm [40] to couple the velocity and pressure. Further details on the numerical settings can be found in **Table 1**. The computational domain comprises nearly 168 million non-uniform grid cells, whose resolution is assessed using various methods, such as two-point correlations [41, 42], Pope grid resolution index using the ratio of resolved kinetic energy (k_{res}) to total turbulent kinetic energy ($TKE_t = (k_{res} + k_{SGS})$) [43], and Celik et al., grid resolution index using effective Kolmogorov length scale and effective viscosity [44].

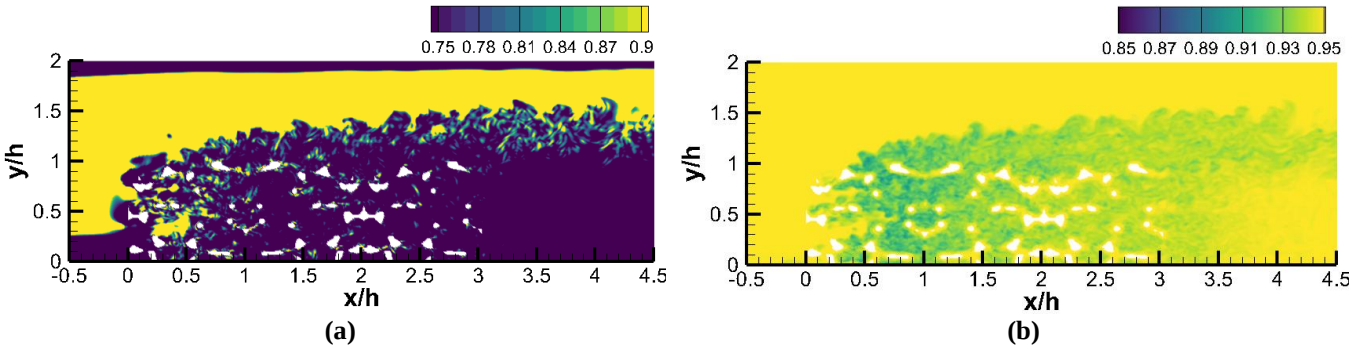

Figure 3. Grid Assessment on the symmetry plane ($z/h = 0$) at Reynolds number $Re_h = 7200$ and porosity of 85% ($\varepsilon = 85\%$), using (**a**) Pope grid resolution index [43] and (**b**) Celik et al. grid resolution index [44].

Analysis of the distribution of k_{res}/TKE_t in **Figure 3** suggests that the current grid resolution captures more

than 80% of the total turbulent kinetic energy and features a filter size almost 8 times larger than the Kolmogorov length scale. The results confirm that the selected grid resolution guarantees a well-resolved Large Eddy Simulation, ensuring an accurate representation of turbulent phenomena in the studied system.

Table 1 Details of the numerical settings in the PISO solver.

Numerical settings	Schemes/Methodology	Description/comments
Pressure-velocity coupling algorithm	PISO algorithm	
Time discretization	Backward scheme	Second-order implicit
Convection term discretization	Central differencing scheme	Unbounded second-order
Divergence term discretization	Bounded central difference scheme	Second-order bounded
Laplacian term discretization	Corrected	Unbounded second-order
Time step size, Δt	$\Delta t/(h/U_{in}) = 1\times10^{-5}$	CFL < 1
Sampling time	$t^* = t \times U_{in}/h = 490$	70 flow-through times

To validate the accuracy of our pore-scale Large Eddy Simulation solver, the velocity and turbulent statistics obtained from our simulations were compared with the experimental measurements of Leu et al. [35]. The comparison was done at two locations, X/D = 1.6 and 3.0, and the results showed good agreement between the first- and second-order statistics of the velocity from the LES calculations and the measured data. **Figure 4** illustrates the comparison of the two datasets. The average and maximum errors for the obtained data at X/D = 1.6 were 16.3% and 27.2%, respectively, while the corresponding errors for the predicted results at X/D = 3.0 were 17.3% and 25.4%.

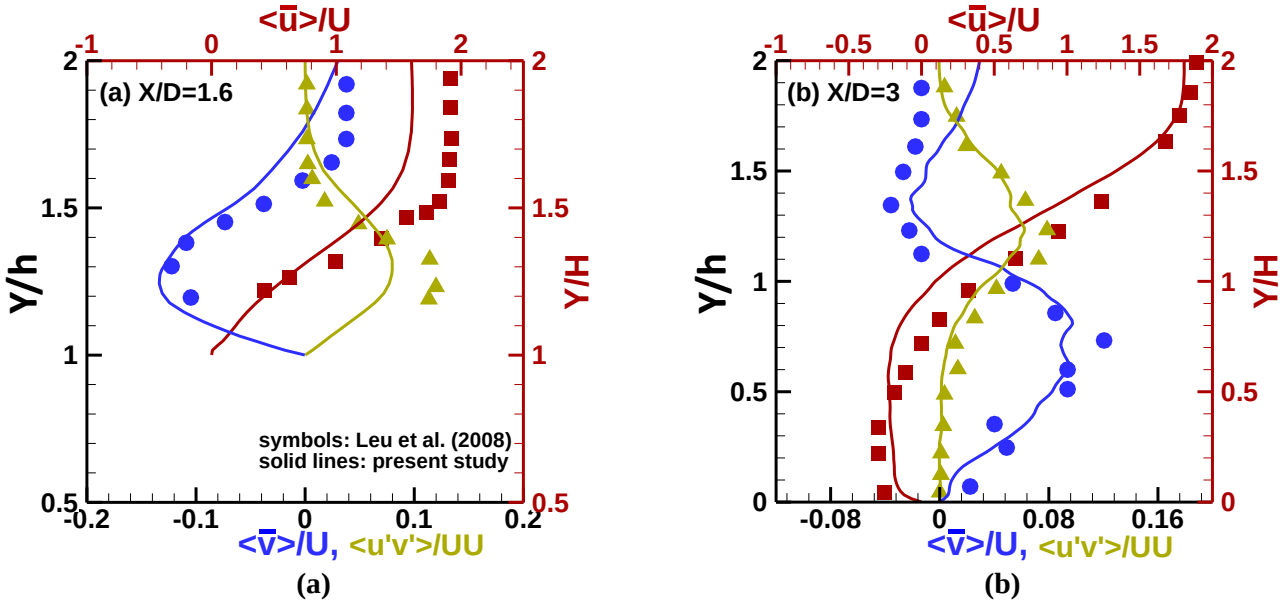

Figure 4. Comparison of first- and second-order velocity statistics obtained from the pore-scale Large Eddy Simulation study with experimental measurements by Leu et al. [35]. The symbol $\langle\ \bar{}\ \rangle$ denotes the time-averaged value of the filtered variable. **(a)** On the interface at X/D = 1.6; **(b)** In the wake region at X/D = 3.0.

2.3 Mathematics of POD for modal analysis

Data-driven decompositions of CFD results are employed for extracting insights from data. The primary objective of any decomposition is to represent the data as a linear combination of fundamental elements known as modes, each possessing distinct spatial structures and temporal evolutions capable of capturing essential features within the data. Comprehensive reviews of data-driven decompositions and modal analysis are available in the works of [45]. The most common approaches can be broadly categorized into two main classes: energy-based and frequency-based decompositions [46]. Energy-based decompositions are employed in the present study, rooted in Proper Orthogonal Decomposition (POD) and its variants, offering the most energetic modes without constraints on their frequency content.

In conjunction with LES, Proper Orthogonal Decomposition proves to be an invaluable technique for extracting flow dominant modes (most energetic modes) and their corresponding frequencies inherent in turbulent flows from the vast and intricate datasets generated by LES. By decomposing the LES data into a reduced set of spatial modes and corresponding temporal coefficients, POD offers a concise and interpretable representation of information transfer between different modes in different regions of the composite porous-fluid system [47, 48]. To state simply, POD re-expresses the original data into a new orthogonal basis, $\varphi_i(\vec{x})$. The turbulent space-time velocity signal, $u_i(\vec{x}, t)$, is characterized by $\mathbb{R}$ spatial-temporal modes which form a complete orthogonal basis for the following expansion:

$$u_i(\vec{x}, t) = \sum_{r=1}^{R} \psi^r(t)\, \phi_i^r(\vec{x}) \tag{4}$$

The temporal modes, $\psi^r(t)$, are the eigenvectors of the temporal correlation tensor, $C(t, t')$.

$$\int_T C(t, t')\psi^r(t')dt' = \sigma^r \psi^r(t) \tag{5}$$

$$C(t, t') = \frac{1}{T}\int_V u_i(\vec{x}, t)\, u_i(\vec{x}, t')\, d\vec{x} \tag{6}$$

The spatial modes, $\phi_i^r(\vec{x})$, are calculated by projecting the velocity fields onto the temporal modes:

$$\psi_i^r(\vec{x}) = \frac{1}{T\sigma^r}\int_T \psi^r(t)\, u_i(\vec{x}, t)\, dt \tag{7}$$

The r^{th} eigenvalue, σ^r, corresponds to the r^{th} POD mode and contains a piece of information about the contribution of the r^{th} mode to the total turbulence kinetic energy. Re-ordering of the eigenvalues in descending order, that is:

$$\sigma^1 > \sigma^2 > \sigma^3 > \ldots > \sigma^n \qquad r = 1,2,3,\ldots,\mathbb{R} \tag{8}$$

reveals the most dominant modes in the flow. These modes are supposed to be coherent and contain the largest portion of TKE. The value of σ^r represents the contribution to TKE. The importance of each eigenvalue is then expressed by its relative contribution to the sum of all eigenvalues.

$$E^r = \frac{\sigma^r}{\sum_{r=1}^{\mathbb{R}} \sigma^r} \times 100\% \tag{9}$$

The eigenvector, $\phi_i^r(\vec{x})$, describes the spatial distribution of the mode in the flow. Each mode has its weight function that is a function of time, represented in Eq. (7) as the expansion coefficient, $\psi^r(t)$.

3 Discussion of results

In the following subsections, we will first examine the instantaneous and mean flow features inside and over the porous blocks. We will then explore the correspondence between flow leakage and residence time in detail. Next, we will explore the pulsatile nature of the flow and categorize different observed states. We will link these states to the states of turbulence identified by correlation coefficients and quadrant analysis. Finally, we will explore the dynamics of momentum and energy exchanges between porous and non-porous regions.

3.1 Flow leakage and residence time

The flow behaviour in and around stochastic metal foams is extremely complex due to the intricate pore structure, which consists of interconnected ligaments and open cells of various shapes and sizes. The size and shape of the ligaments that form the walls of the open cells have a significant impact on the flow patterns and heat transfer characteristics within the foam. As shown in **Figure 5**, the flow through the stochastic metal foam is subject to two main phenomena: positive flow leakage and a channelling effect. Positive flow leakage occurs when the fluid enters the porous block from the leading face on the stagnation region of the porous block and exits through preferential pathways across the porous-fluid interface, leading to non-uniform flow distribution and reduced residence time of the fluid within the porous block (see **Figure 5(a-b)**). The channelling effect, on the other hand, refers to the formation of high-momentum preferential flow channels within the porous block, which results in localized jet-like flows (see **Figure 5(c-d)**). The contour of streamwise velocity also shows how pore flow exits from the trailing face of the porous block and penetrates the wake region.

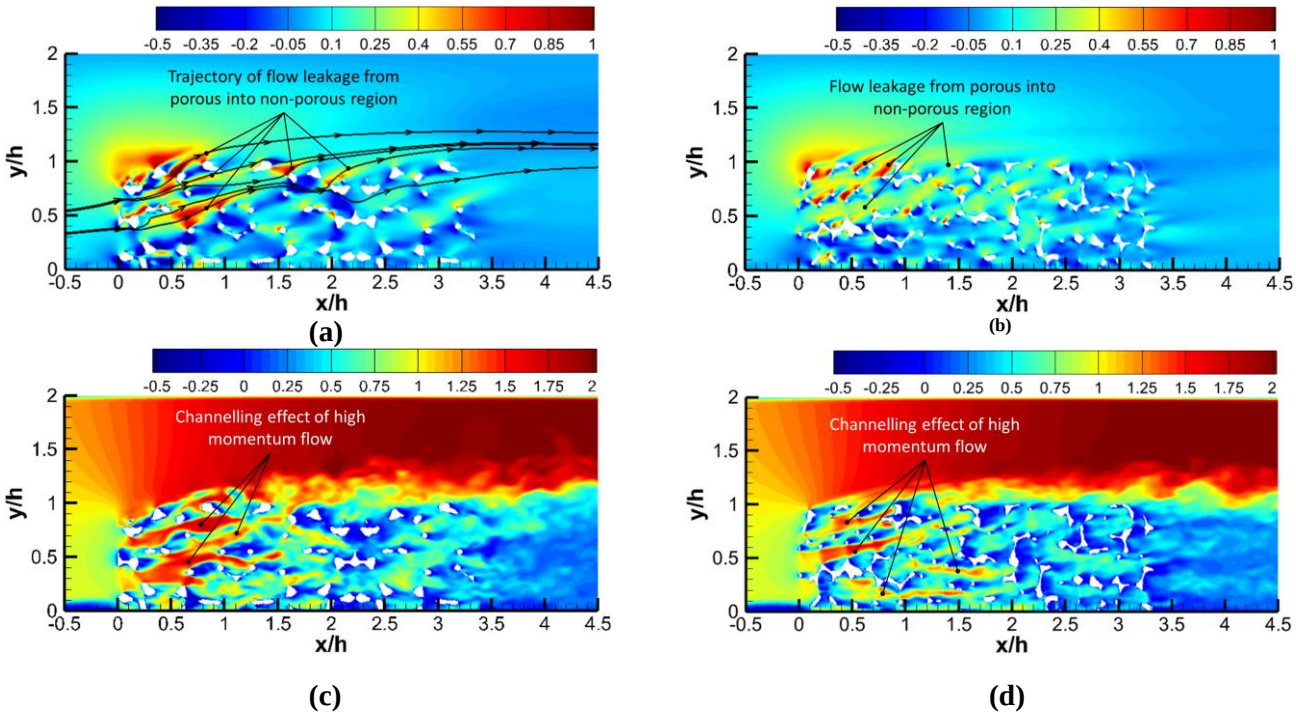

Figure 5. Contour of non-dimensional **(a-b)** time-averaged vertical velocity ($\langle\bar{v}\rangle/U_{in}$) and **(c-d)** instantaneous streamwise velocity ($\langle u\rangle/U_{in}$) at symmetry plane ($z/h = 0$) for for at Re_h = 7200. **Left**: Low porosity; **Right**: High porosity.

Figure 6 shows the positive iso-surface of time-averaged vertical velocity ($\bar{v}/U_{in} = 0.15$) and streamlines for Re_h = 7200. The foremost discernible characteristic is the occurrence of positive flow leakage, where a certain amount of fluid penetrating the porous blocks is directed upwards towards the porous-fluid interface, subsequently departing the porous medium and entering the non-porous region. This phenomenon is further illustrated by the positive iso-surface of time-averaged vertical velocity in **Figure 6**. The presence of positive flow leakage emerges as a critical factor influencing the residence time of fluid. Through our investigation, it has been observed that the presence of positive flow leakage significantly reduces the duration for which the fluid remains confined within the porous block. This effect occurs as the fluid leaks out of the system, leading to a shortened residence time. For instance, in the case of high porosity at Re_h = 7200 and Re_h = 1800, The residence times for a case with flow leakage, compared to the case where no flow leakage occurs ($1/N \times \sum_i^N \frac{1-\forall_i/(Q_{in}^{Porous}-Q_{leak}^{Porous})_i}{(\forall_{total}/Q_{in,NoLeak}^{Porous})}$), decrease by 57.6% and 54.7% respectively. Similarly, for low porosity cases at the same Re_h values, the reduction in residence times is 57.4% and 55.3% respectively. In the above equation, N represents the number of porous length divisions, each with a corresponding volume $\forall_i$. Q_{in}^{Porous} denotes the flow rate entering that particular portion of the porous block,

while Q_{leak}^{Porous} signifies the flow leakage from that specific segment of the porous block. $\forall_{total}$ refers to the total volume of the porous block, and $Q_{in,NoLeak}^{Porous}$ represents the overall flow rate passing through the porous block without any leakage. These findings emphasize the importance of considering flow leakage when analyzing the behaviour and performance of porous block configurations, as it directly influences the temporal dynamics and fluid exchange processes within the system.

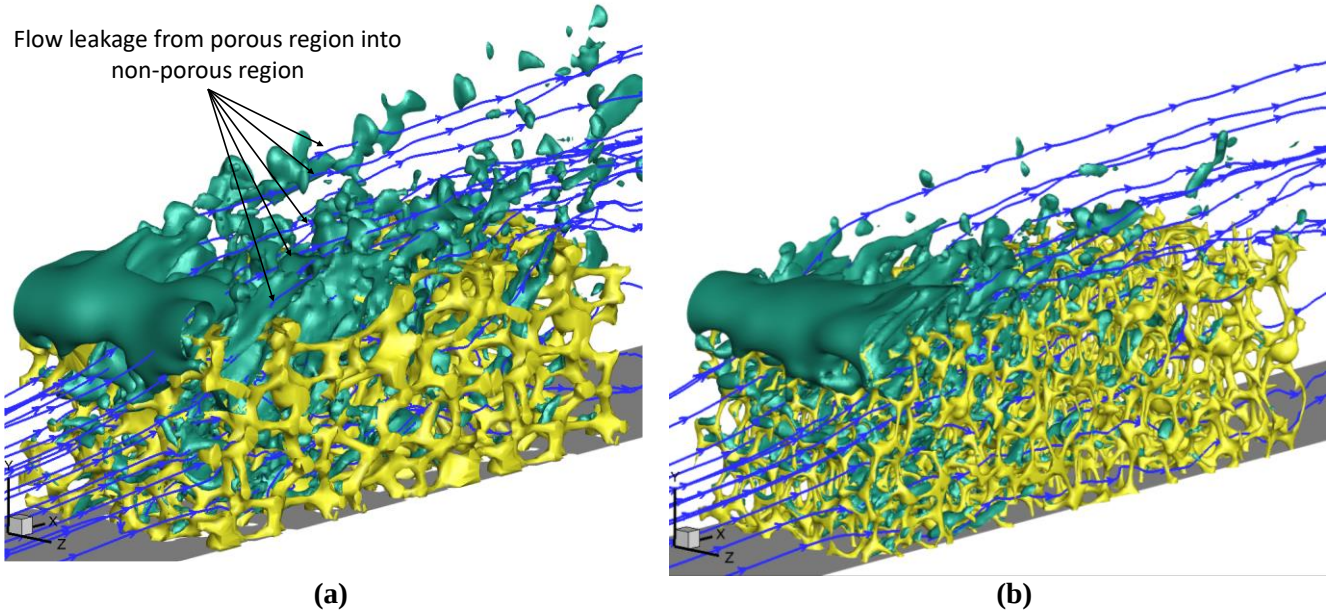

Figure 6. Iso-surface of non-dimensional time-averaged vertical velocity ($\bar{v}/U_{in} = 0.15$) at Re_h = 7200; Streamlines show how the flow leaks from the porous region into the non-porous region. Positive flow leakage leads to a reduction in the residence time of fluid within the porous block. **(a)** Low porosity (ε = 85%); **(b)** High porosity (ε = 91%).

Table 2 shows the flow rates that leak from the porous region and enter the non-porous region, both in absolute and relative terms. A parameter, $Q_{in}^{Porous} = \int_0^h \int_{-0.65h}^{0.65h} < \bar{u}(y,z) > dzdy$, is introduced to calculate the time-averaged flow rate that penetrates the porous block from its windward face, while $Q_{lx}^{Porous} = \int_0^X \int_{-0.65h}^{0.65h} < \bar{v}(x,z) > dz\,dx$ is the time-averaged flow rate that leaks from the X-percentage of the porous-fluid interface. **Table 2** provides evidence that an increase in the Reynolds number results in a higher absolute flow rate entering the porous block, but approximately 37% of the inlet flow always penetrates the porous block, regardless of the Reynolds number, while the remaining flow passes over the free area above the block. The trend of $Q_{lx}^{Porous}/Q_{in}^{Porous}$ at various streamwise locations indicates a gradual decrease in positive flow leakage from the leading edge to the trailing edge of the porous block. For all Reynolds numbers, over 50% of the flow entering the porous block exits from the porous interface before x/L = 0.6,

and this becomes more pronounced at lower Reynolds numbers. As positive flow leakage gradually decreases from the leading edge towards the trailing edge of the porous block, a dissimilar information transfer is anticipated between the porous and non-porous regions along the length of the porous block.

Table 2. Relative values of flow rate that leaks from the porous region into the non-porous region.

	x-position along the porous-fluid interface	Low porosity		High porosity	
		Re_h = 1800	Re_h = 7200	Re_h = 1800	Re_h = 7200
$Q_{in}^{Porous} \times 10^{-3}\ [m^3/s]$		8.08	32.57	8.21	33.34
$Q_{lx}^{Porous}/Q_{in}^{Porous} \times 100$	$x = 0.2$L	30.11	29.36	29.35	27.74
$Q_{lx}^{Porous}/Q_{in}^{Porous} \times 100$	$x = 0.4$L	44.35	42.77	47.09	44.41
$Q_{lx}^{Porous}/Q_{in}^{Porous} \times 100$	$x = 0.6$L	55.32	53.28	55.34	52.55
$Q_{lx}^{Porous}/Q_{in}^{Porous} \times 100$	$x = 0.8$L	62.94	60.71	63.05	60.20
$Q_{lx}^{Porous}/Q_{in}^{Porous} \times 100$	$x = 1.0$L	66.72	64.21	67.33	64.33

Figure 7 displays the contour of non-dimensional time-averaged vertical velocity along with the probability density functions (PDFs) of vertical velocity for five sampling points (Probes #1-5). The PDF distribution for Probe #1, located within the porous region in the path of positive flow leakage at x/h = 1.22 and y/h = 0.76, is left-skewed, indicating a high tendency of positive flow leakage inside the porous region. The time-averaged vertical velocity at this location is 0.13, with a probability of being negative of less than 8%. The left-skewed PDF for Probe #4, located at the porous-fluid interface at x/h = 1.67 and y/h = 1.0, reveals positive flow leakage across the interface, with a probability of flow penetration from the non-porous region to the porous region of less than 5%. Due to the contraction of the flow area by the porous ligaments, the contour of vertical velocity at this location shows flow acceleration, resulting in high-momentum positive flow leakage across the interface. At the end of the porous block, where the positive flow leakage is negligible, the PDF of vertical velocity for Probe #5 on the interface at x/h = 2.9 and y/h = 1.0 displays nearly Gaussian distribution, with a chance of flow penetration from the non-porous region to the porous region and positive flow leakage of 41% and 59%, respectively. The low magnitude of time-averaged vertical velocity at this location confirms the negligible positive flow leakage, as shown in **Table 2**. For Probes #2 (at x/h = 1.0 and y/h = 1.0) and #3 (at x/h = 1.45 and y/h = 1.0), located in the wake of porous ligaments on the interface, the PDF distribution is right-skewed, indicating a strong probability of negative vertical velocity values, signifying flow penetration from the non-porous to the porous area, named as a negative flow leakage. Hence, in the wake of a ligament on the interface, the flow in the non-porous region tends to enter the porous region.

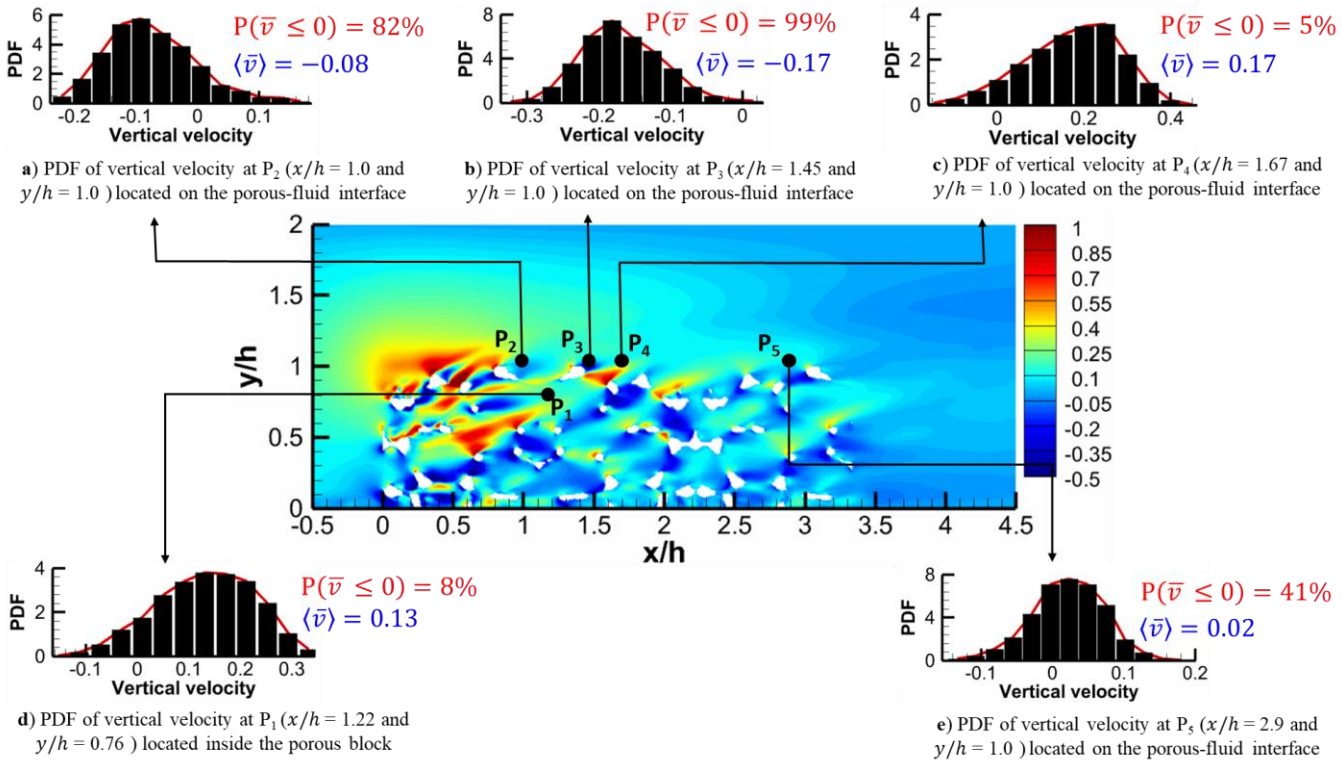

a) PDF of vertical velocity at P_2 ($x/h = 1.0$ and $y/h = 1.0$) located on the porous-fluid interface

b) PDF of vertical velocity at P_3 ($x/h = 1.45$ and $y/h = 1.0$) located on the porous-fluid interface

c) PDF of vertical velocity at P_4 ($x/h = 1.67$ and $y/h = 1.0$) located on the porous-fluid interface

d) PDF of vertical velocity at P_1 ($x/h = 1.22$ and $y/h = 0.76$) located inside the porous block

e) PDF of vertical velocity at P_5 ($x/h = 2.9$ and $y/h = 1.0$) located on the porous-fluid interface

Figure 7. Contour shows the non-dimensional time-averaged vertical velocity ($\langle\bar{v}\rangle/U_{in}$) at symmetry plane ($z/h = 0$) at Re_h = 7200 for the low porosity (ε = 85%) case; The bar chart shows the probability density function (PDF) of vertical velocity at 5 probes to analyse the momentum exchange between porous and non-porous regions. The P_1 probe is in the porous region and the other probes ($P_{2\text{-}5}$) are located on the porous-fluid interface; For each PDF bar chart, $P(\bar{v} \leq 0)$ represents the probability of a negative vertical velocity; $\langle\bar{v}\rangle$ shows the time-averaged value of the filtered vertical velocity.

3.2 Modal analysis

3.2.1 Spatial modes

The application of the snapshot Proper Orthogonal Decomposition (POD) technique, as detailed in sub-section 2.3, is utilized to examine the modes of Large-Eddy Simulation (LES) outcomes within the symmetry plane at $z/h = 0$ and off symmetry plane at $z/h = 0.1$. This analysis focuses on four POD zones between $0 \leq x/h \leq 3.0$ and $0 \leq y/h \leq 1.5$, as depicted in **Figure 8**. The first POD region (POD01) is positioned at the initial segment of the porous block between $0 \leq x/h \leq 1.0$ and $0 \leq y/h \leq 1.0$, where flow leakage is significant. The second POD zone (POD02) is situated in the central part of the metal foam between $1.0 \leq x/h \leq 2.0$ and $0 \leq y/h \leq 1.0$, characterized by low flow leakage, and the third POD zone (POD03) is located at the end of the porous block between $2.0 \leq x/h \leq 3.0$ and $0 \leq y/h \leq 1.0$, where flow leakage is negligible. The fourth POD zone (ShearPOD) is placed over the porous-fluid interface in the shear layer above the porous block between $0 \leq x/h \leq 3.0$ and $1.0 \leq y/h \leq 1.5$. These POD zones

have been selected based on the flow leakage information listed in **Table 1**. By subdividing the porous block into three zones, we can systematically investigate the POD modes interactions and transfer of flow across each zone in the porous region with the shear layer above the porous-fluid interface in the non-porous region. Furthermore, the computational cost of the modal analysis can be effortlessly managed. Each POD zone in the porous block consists of 27,556 monitoring points distributed uniformly in both the vertical and streamwise directions (see **Figure 8**). The POD zone over the porous-fluid interface in the shear layer consists of 43,086 monitoring points arranged in the streamwise direction and the vertical direction. For this POD zone, the number of points in the streamwise direction is $N_x = 501$, and in the vertical direction, it is $N_y = 86$. The distance between the monitoring points is uniform and equal to $0.006h$. The velocity components at the monitoring points are sampled at a frequency of $f_s =$ 500 Hz ($\Delta t^* = 2.0\times10^{-3}$).

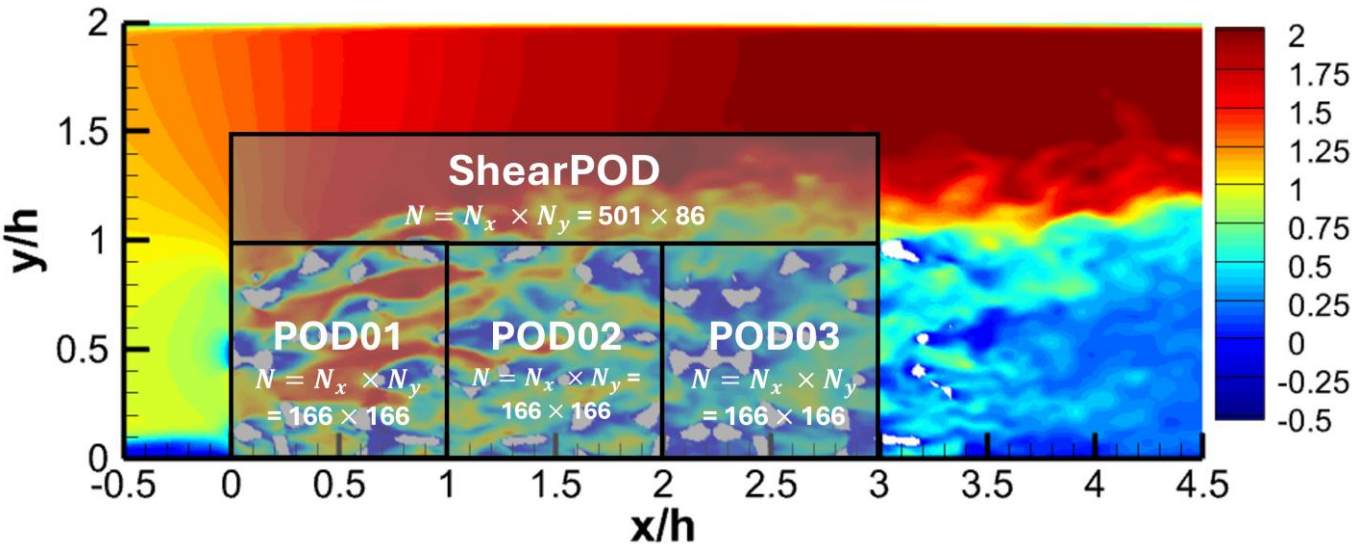

Figure 8. Illustration of POD zones on the instantaneous contour of streamwise velocity for low porosity case at Re_h = 7200 on the symmetry plane ($z/h = 0$); The POD zones are positioned between $0 \leq x/h \leq 3.0$ and $1.0 < y/h \leq 1.5$ and the designation of these POD zones is predicated upon the flow leakage data delineated in **Table 1**; The distance between the monitoring points for all the zones is uniform and equal to $0.006h$.

For each specific POD zone, 4000 snapshots are utilized in the POD analysis. To explore the impact of varying the number of snapshots, the POD analysis is conducted for 3000, 4000, and 5000 snapshots. The resulting POD modes and their corresponding coefficients exhibit nearly identical patterns across these three datasets, with only minor, random differences observed in the higher POD modes. Consequently, the use of 4000 snapshots is deemed sufficient to ensure a reasonable level of accuracy in the present POD analysis. The time equivalent to a duration of 4000 snapshots is 8 dimensionless time units, denoted as $t^* = t \times U_{in}/h$. These 8 dimensionless time durations signify the period during which the mean flow traverses

the entire length of the porous blocks 3.2 times.

As detailed in sub-section 2.3, the eigenvalue, σ, denotes the respective contribution of each Proper Orthogonal Decomposition (POD) mode to the overall turbulence kinetic energy. The bar charts in **Figure 9** are the distribution of the percentage of total fluctuating energy attributed to each POD mode for the POD01 and ShearPOD zones. For the ShearPOD zone, the initial 100 POD modes contribute 35.1% to the total fluctuating energy, respectively, with a gradual decline to 18.6% for mode 20. The contribution of the first mode is 1.3%. A comparative analysis of contributions to turbulent kinetic energy reveals that, for the ShearPOD zone, the first 100 POD modes account for 35.1%, whereas the POD01 zone indicates a higher percentage of 59.4%.

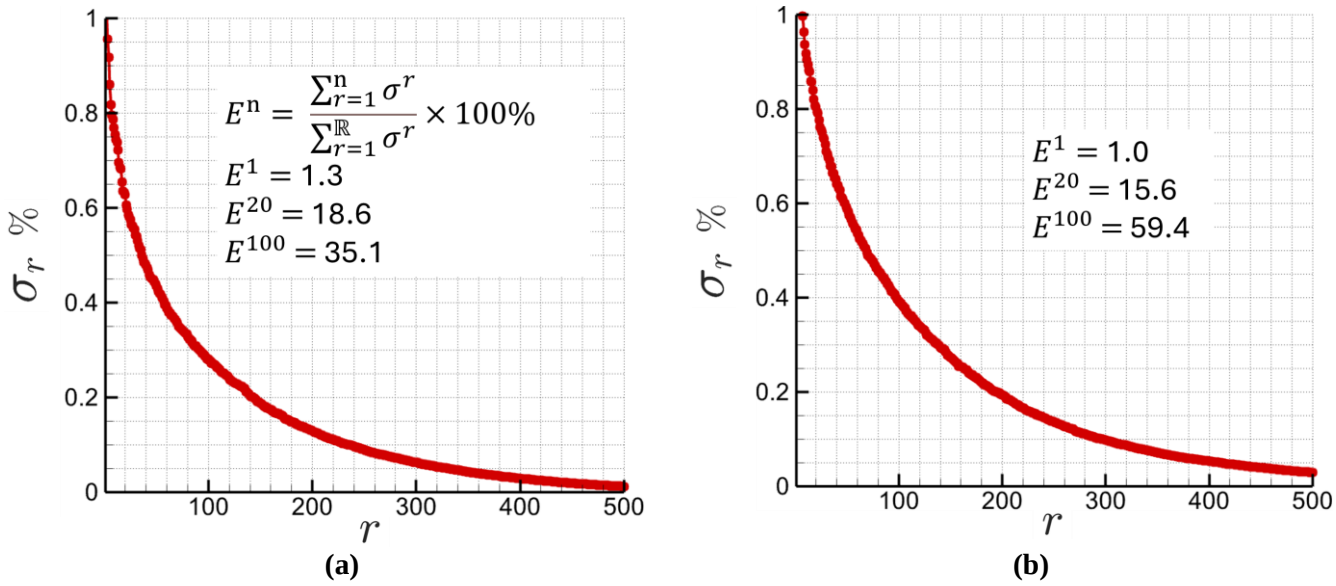

Figure 9. Quantifying the fractional contribution of individual POD modes to the total turbulence kinetic energy across various POD zones. **(a)** ShearPOD zone; **(b)** POD01 zone.

In subsequent discussions, our attention is directed towards the initial 20 POD modes. The spatial eigenvectors, $\varphi_i^n(\vec{x}), i = 1, 2$ are linked to the velocity components, $u(\vec{x}, t)$ and $v(\vec{x}, t)$, represent the separate contribution of each mode to the spatial structure of the streamwise and vertical components of the velocity field. **Figure 10** shows the three POD modes of the streamwise and vertical velocity components by vectors and their magnitude by the contour in the ShearPOD zone. The vectors offer a clear depiction of the velocity field's direction for each specific mode, aiding in the identification of key flow patterns. Additionally, the contour is utilized to illustrate the magnitude of the modes enabling a detailed examination of the intensity of flow within these specific zones. In **Figure 10** the spatial structures on the porous-fluid interface at $y/h = 1.0$ reveals a distinct alternation of zones, characterized by either upward (positive vertical

velocity) or downward (negative vertical velocity) vectors. The colour bar situated above the horizontal axis of the figure presents two colours: red signifies regions on the porous-fluid interface exhibiting positive flow leakage from the porous region, while blue highlights areas with negative flow leakage into the porous region. The vertical velocity components of modes 1, 6, and 11 validate the presence of both positive and negative flow leakage, indicating dynamic momentum exchange between the porous and non-porous regions across the porous-fluid interface. This phenomenon is consistently observed across all modes of spatial structures. The positive and negative flow leakage across the interface is further explored by spectral analysis in subsection 3.3.

Figure 11 displays spatial structures for modes 1 and 6 in the POD01, POD02, and POD03 zones. The vectors represent the streamwise and vertical velocity components of the modes, while the contours depict the magnitude of the modes. The utilization of POD within the designated zones serves as a powerful tool for isolating prevailing spatial structures, setting them apart from the mean flow features illuminated in Mode = 0, as comprehensively discussed in **Figure 5**.

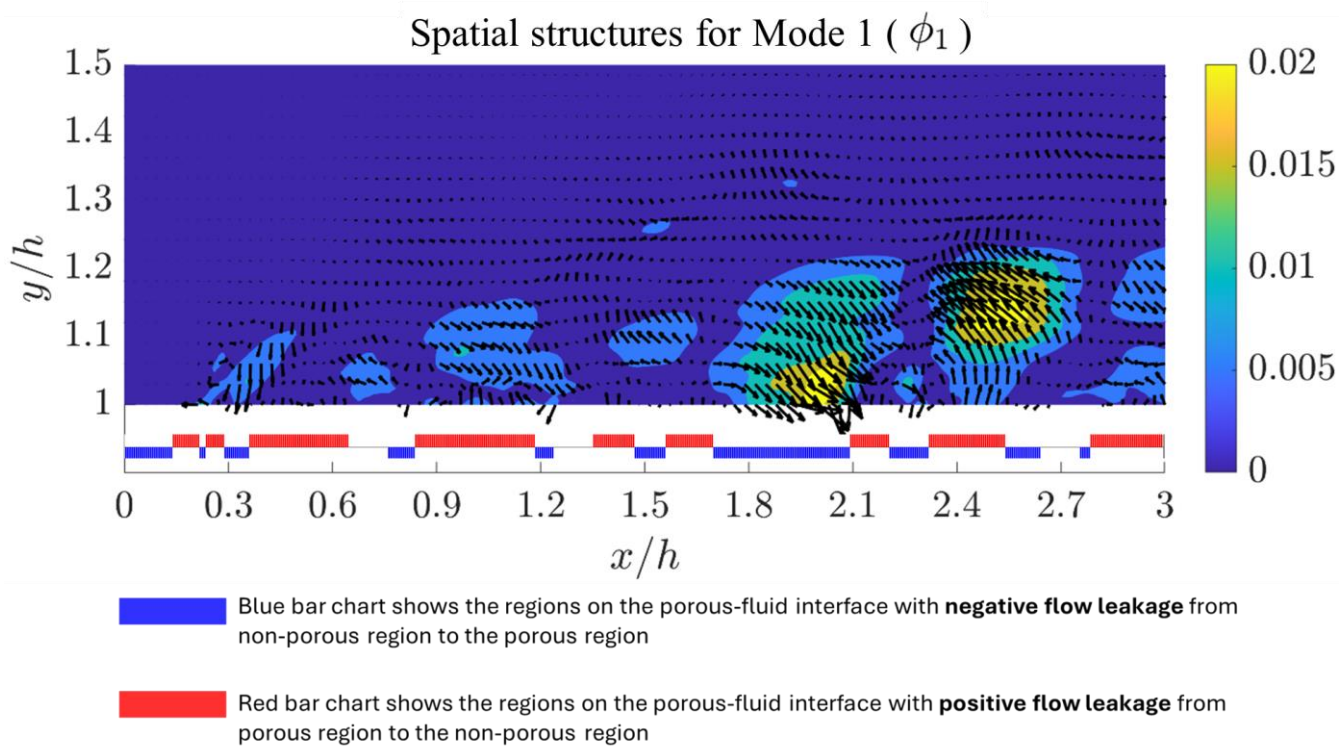

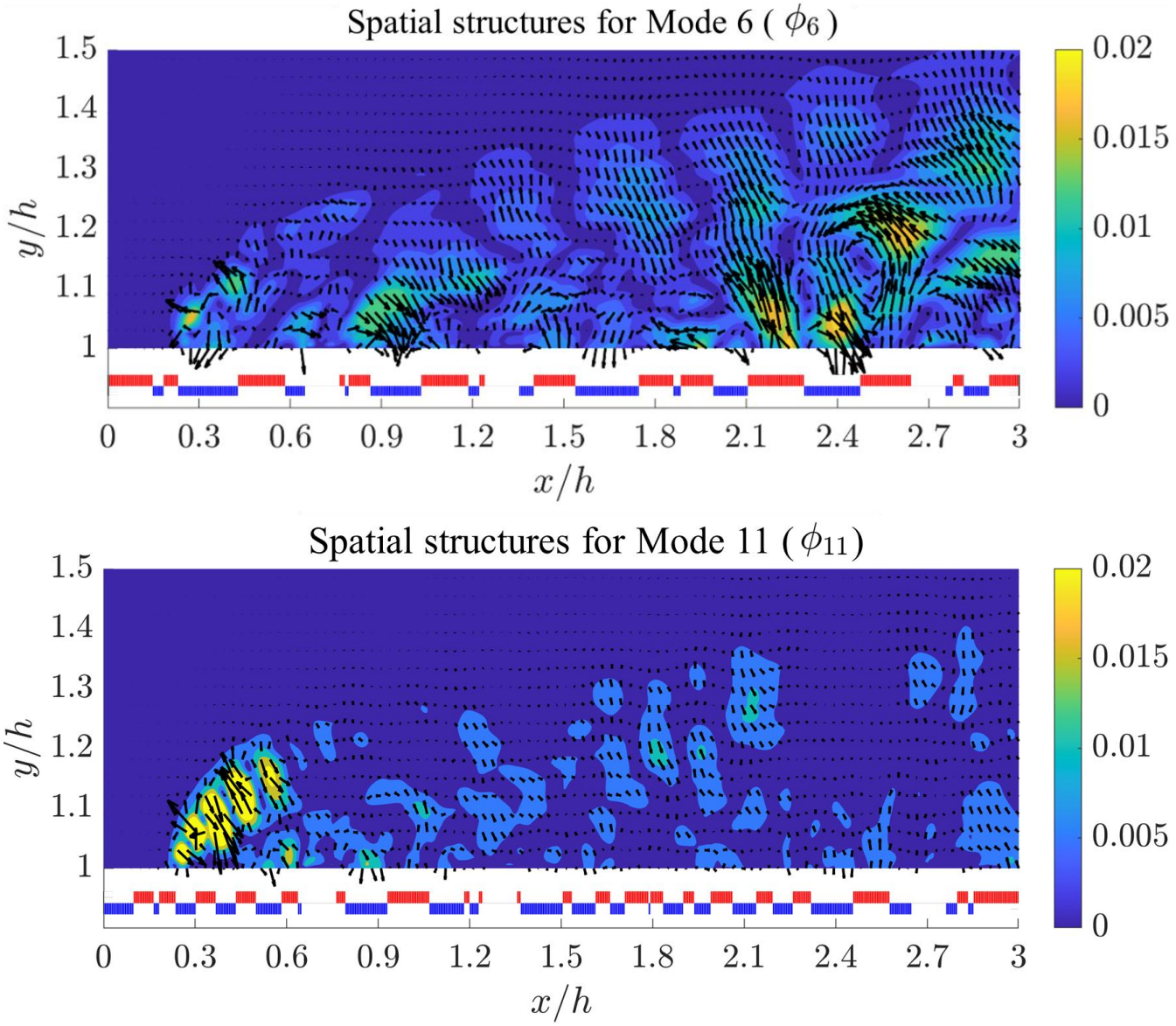

Figure 10. Vector representation of streamwise (φ_u) and vertical (φ_v) velocity component of modes 1, 6 and 11 in the ShearPOD zone at the plane of symmetry (z/h = 0.1); The contour shows the magnitude of streamwise and vertical component ($\varphi = \sqrt{\varphi_u^2 + \varphi_v^2}$) of modes; The colour bar in the top figure shows the regions in the porous-fluid interface for positive (red colour) and negative (blue colour) flow leakage; **Top**: Mode 1; **Middle**: Mode 6; **bottom**: Mode 11.

This approach allows for a more nuanced understanding of the flow dynamics within the porous region. **Figure 11** visually captures this complexity, revealing a spatial flow structure that encompasses a spectrum of flow characteristics, including upward, downward, forward, and backward motions.

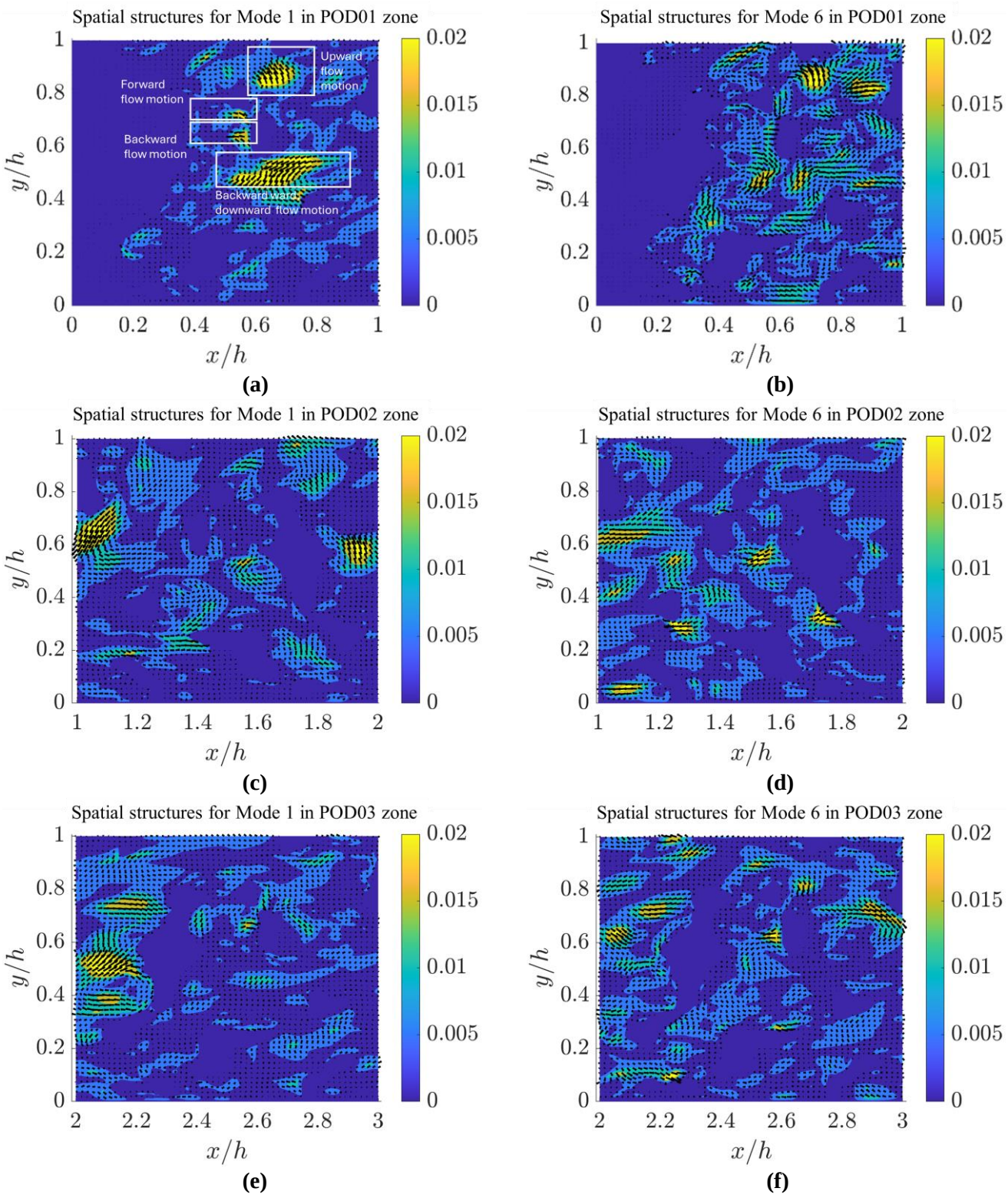

Figure 11. Vector representation of streamwise and vertical velocity component of mode 1 (**Left**) and mode 6 (**Right**) in the three POD zones inside the porous region at the plane of symmetry ($z/h = 0$); **Top**: POD01 zone; **Middle**: POD02 zone; **bottom**: POD03 zone.

Drawing a comparison with the analysis of mean streamwise and vertical flow (mode = 0) presented in **Figure 5**, which predominantly showcases upward and forward flow within the POD01 zone, the subsequent examination in **Figure 11**(**a-b**) delves into the rich intricacies of modes 1 and 6. These modes exhibit flow patterns extending in all directions, demonstrating the diverse nature of the flow dynamics within the porous medium. Notably, the presence of such complex flow patterns challenges the conventional notion of unidirectional flow within porous materials discussed in **Figure 5** by the mean flow. This observation suggests that while the mean flow (Mode = 0) serves as the primary conduit for information transfer, facilitating momentum exchange and heat transfer from the porous to the non-porous region through upward and forward flow motions, the turbulent fluctuations inherent in other POD modes (Mode ≠ 0), exemplified by modes 1 and 6 in **Figure 11**(**a-b**), contribute to information transfer across a spectrum of directions. This multifaceted understanding sheds light on the comprehensive role that spatial structures and turbulent fluctuations play in shaping the turbulent momentum exchange within the stochastic metal foam.

3.2.2 Temporal modes and frequency analysis

Figure 12 depicts the temporal evolution of the modes $\psi^r(t)$ and corresponding frequency spectra, $\hat{\psi}^r(f)$, for 6 dimensionless time units, $t^* = t \times U_{in}/h$. Time records of temporal modes at POD zones in the porous regions for different modes show positive and negative values that indicate the information transfer across a spectrum of directions at different times. This understanding reveals the intricate motion of spatial structures by turbulent fluctuations, shedding light on their comprehensive role in shaping turbulent momentum exchange within the stochastic metal foam. Time records of temporal modes within the POD zones in the porous regions in **Figure 12**(**a, e, i**), reveal both positive and negative values. These values signify the transfer of information occurring across a diverse range of directions at different instances in time. The temporal analysis adds a dynamic dimension to the exploration, highlighting how the information transfer manifests and evolves over time, contributing to a more nuanced comprehension of the fluid dynamics within the porous medium. The $\hat{\psi}^r(f)$ of the modes in **Figure 12** show a distinct peak at different Strouhal numbers ($St = fh/U_{in}$ where "f" is frequency). **Table 3** complements these observations by presenting the dominant Strouhal numbers for the initial 10 modes within both the ShearPOD and POD01 zones. For example, for the ShearPOD zone, the St in first row and column shows that for the first mode, the first dominate Strouhal number is St_1^1 = 1.1 where the subscript shows the index of mode, and the superscript shows the index of dominant frequency. For the POD01 zone, St_1^1 = 0.4.

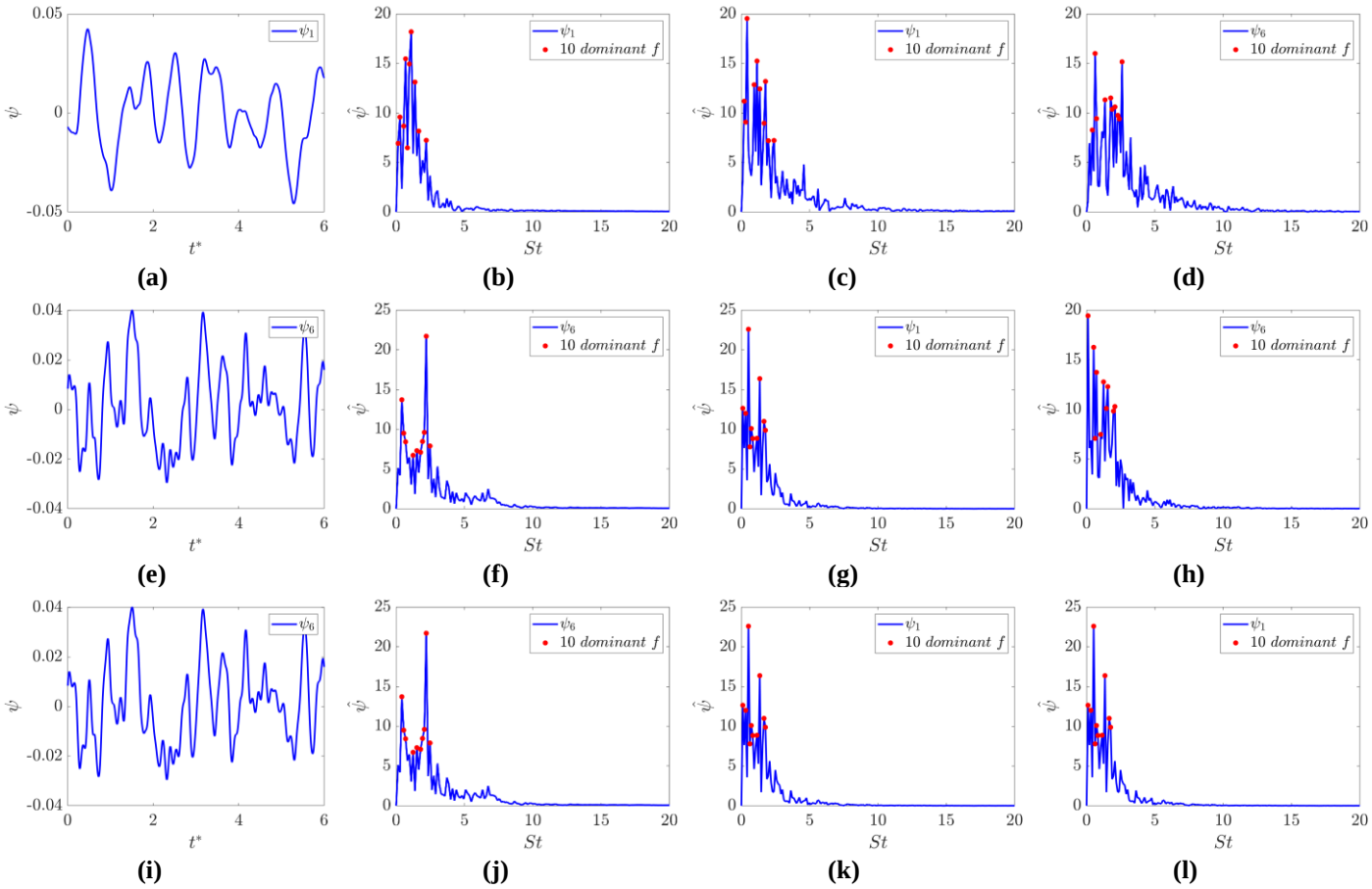

Figure 12. Time records and spectra of temporal modes at POD zones for different modes; **First column**: Time records of temporal mode 1, 6, and 11 at the ShearPOD zone; **Second column**: Spectra of temporal mode 1, 6, and 11 at the ShearPOD zone; **Third column**: Spectra of temporal mode 1 at POD01, POD02, and POD3 zones; **Fourth column**: Spectra of temporal mode 6 at POD01, POD02, and POD3 zones.

The examination of dominant Strouhal numbers (St) in the ShearPOD and POD01 zones, as detailed in **Table 3**, reveals a noteworthy phenomenon. Specifically, certain frequencies within the POD01 zone, situated within the porous region, coincide with frequencies observed in the ShearPOD zone located in the non-porous region. For instance, $St_3^4 = 1.8$ (highlighted in black in **Table 3**) is not only present in other modes within the POD01 zone (highlighted in blue) but also manifests in the ShearPOD zone across different modes (highlighted in green). This observation aligns with our earlier discussion in **Figure 10**, where we explored the turbulent momentum exchange dynamics at the porous-fluid interface. The simultaneous existence of dominant Strouhal numbers in both porous and non-porous regions, as apparent in **Table 3**, substantiates the active momentum exchange occurring between different modes within these distinct regions. This coexistence of frequencies emphasizes the intricate interplay and dynamic interaction between the porous and non-porous domains, further confirming the comprehensive understanding of

turbulent momentum exchange dynamics articulated in our prior analyses.

Table 3. The 10 dominant Strouhal numbers ($St = fh/U_{in}$ where "f" is frequency) among the initial 20 modes in the POD zones.

Index of mode	Index of dominant St in the ShearPOD zone									
	1	**2**	**3**	**4**	**5**	**6**	**7**	**8**	**9**	**10**
1	1.1	0.7	1.0	1.4	0.3	0.5	1.6	2.2	0.1	0.8
2	1.1	0.7	1.4	1.0	0.5	2.2	1.6	1.5	1.8	0.8
3	0.1	1.6	1.2	1.8	0.3	1.5	0.7	0.8	0.5	0.4
4	1.6	1.8	2.2	0.7	1.2	0.4	0.5	1.0	2.1	1.1
5	0.1	1.6	1.2	0.5	0.4	1.0	0.3	1.8	0.8	1.1
6	2.2	0.4	2.1	0.5	1.9	0.7	2.5	1.5	1.8	1.2
7	1.9	3.0	2.2	1.8	2.1	1.1	3.7	2.7	1.5	1.0
8	1.5	0.4	2.7	3.0	3.8	0.7	1.1	2.5	3.2	0.8
9	2.2	2.5	1.5	1.2	2.7	2.3	0.7	0.3	1.9	3.0
10	1.9	1.0	3.0	2.2	2.9	2.6	2.7	1.5	0.3	0.4

Index of mode	Index of dominant St in the POD01 zone									
	1	**2**	**3**	**4**	**5**	**6**	**7**	**8**	**9**	**10**
1	0.4	1.1	1.8	0.9	1.4	0.2	0.3	1.7	2.4	2.0
2	1.8	1.2	0.7	1.7	0.1	0.4	0.6	0.2	1.4	1.1
3	0.9	0.1	0.7	0.5	0.3	0.4	2.5	2.3	1.8	1.1
4	0.2	0.7	1.9	0.4	2.0	1.4	2.5	1.0	0.3	1.2
5	0.2	0.4	0.6	1.5	0.9	0.7	1.6	2.5	2.0	0.3
6	0.6	2.6	1.8	1.4	2.1	1.9	2.3	0.7	2.4	0.4
7	2.5	0.5	2.3	1.5	2.8	1.1	2.6	0.9	0.2	1.8
8	0.9	0.2	1.6	1.9	0.7	3.3	0.6	1.5	1.0	1.4
9	2.3	1.0	0.3	0.5	1.6	0.6	1.2	1.1	0.1	0.8
10	0.3	1.0	2.4	2.3	0.7	1.1	0.2	0.9	3.1	1.9

To systematically investigate the interaction of dominant frequencies between the POD01, POD02, and POD03 zones within the porous region and the 20 initial modes in the ShearPOD zone within the non-porous region, the frequency contents of each mode in the porous region are compared with the frequency contents of the modes in the non-porous region, as illustrated in **Figure 13**. **Figure 13(a, c, e)** shows the co-occurrence of dominant frequencies of the first mode in POD01, POD02, and POD03 zones with all 20 initial modes in the ShearPOD zone. The non-zero elements in **Figure 13(a, c, e)** indicate that one of the 10 dominant frequencies in mode 1 of POD01, POD02, and POD03 zones is observed in the ShearPOD zone, respectively. For example, in **Figure 13(a)**, the $St_1^1 = 1.8$, $St_1^4 = 1.4$ and $St_1^5 = 0.3$ in mode 1 of ShearPOD zone interact with the 10 dominant frequencies of mode 1 in the POD01 zone. Similarly, **Figure 13(c)** demonstrates that the $St_2^1 = 1.1$, $St_2^2 = 0.7$, $St_2^5 = 0.5$, $St_2^9 = 1.8$ and $St_2^{10} = 0.8$ in mode 2 of ShearPOD zone interact with the 10 dominant frequencies of mode 1 in the POD02 zone. **Figure 13(b, d, f)** illustrate

the total co-occurrence of all the initial 20 modes in POD01, POD02, and POD03 zones with all 20 initial modes in the ShearPOD zone. For instance, **Figure 13(b)** shows that $St_1^1 = 0.4$ in the POD01 zone is observed 7 times in all the modes of the ShearPOD zone. Another example is $St_1^5 = 1.4$ in **Figure 13(b)**, which demonstrates that the 5th dominated frequency in mode 1 of the POD01 zone is observed 4 times in all modes of the ShearPOD zone.

Figure 13 reveals that the modes in the porous region interact with the modes in the non-porous region. A comparison of heatmaps in **Figure 13(b, d, f)** discloses that at the beginning of the porous block (POD01 zone), where flow leakage is significant, there are higher values for dominant frequencies interaction between porous and non-porous regions, while it is reduced in the middle (POD02 zone) and end (POD03 zone) sections of the porous region. This data-driven analysis provides a comprehensive understanding of how dominant frequencies dynamically interact across different zones, shedding light on the turbulent interplay between the porous and non-porous regions.

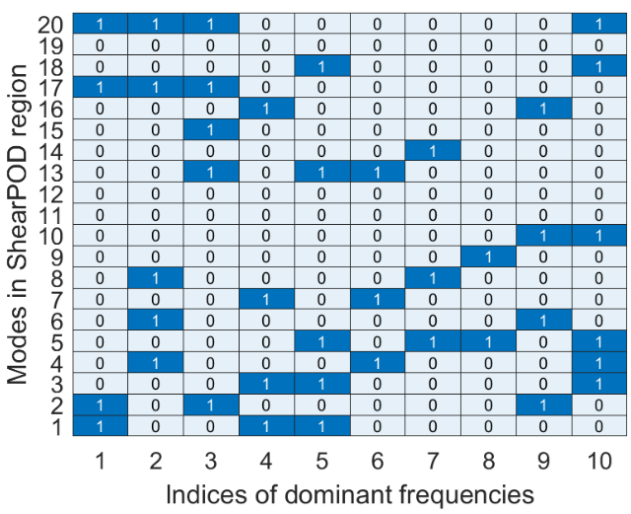

(a)

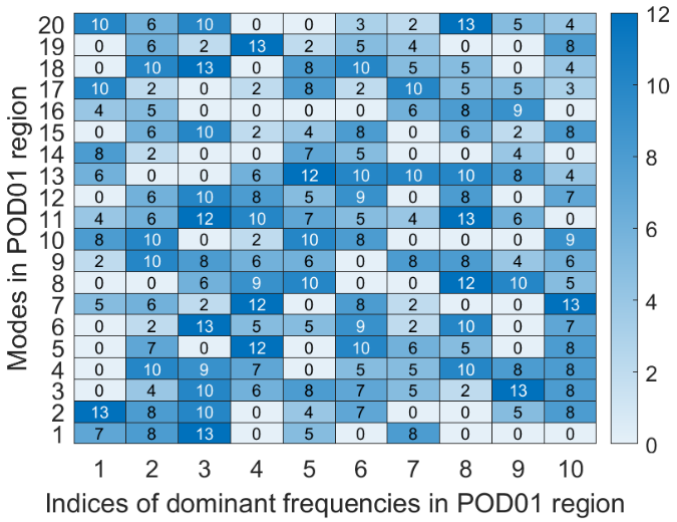

(b)

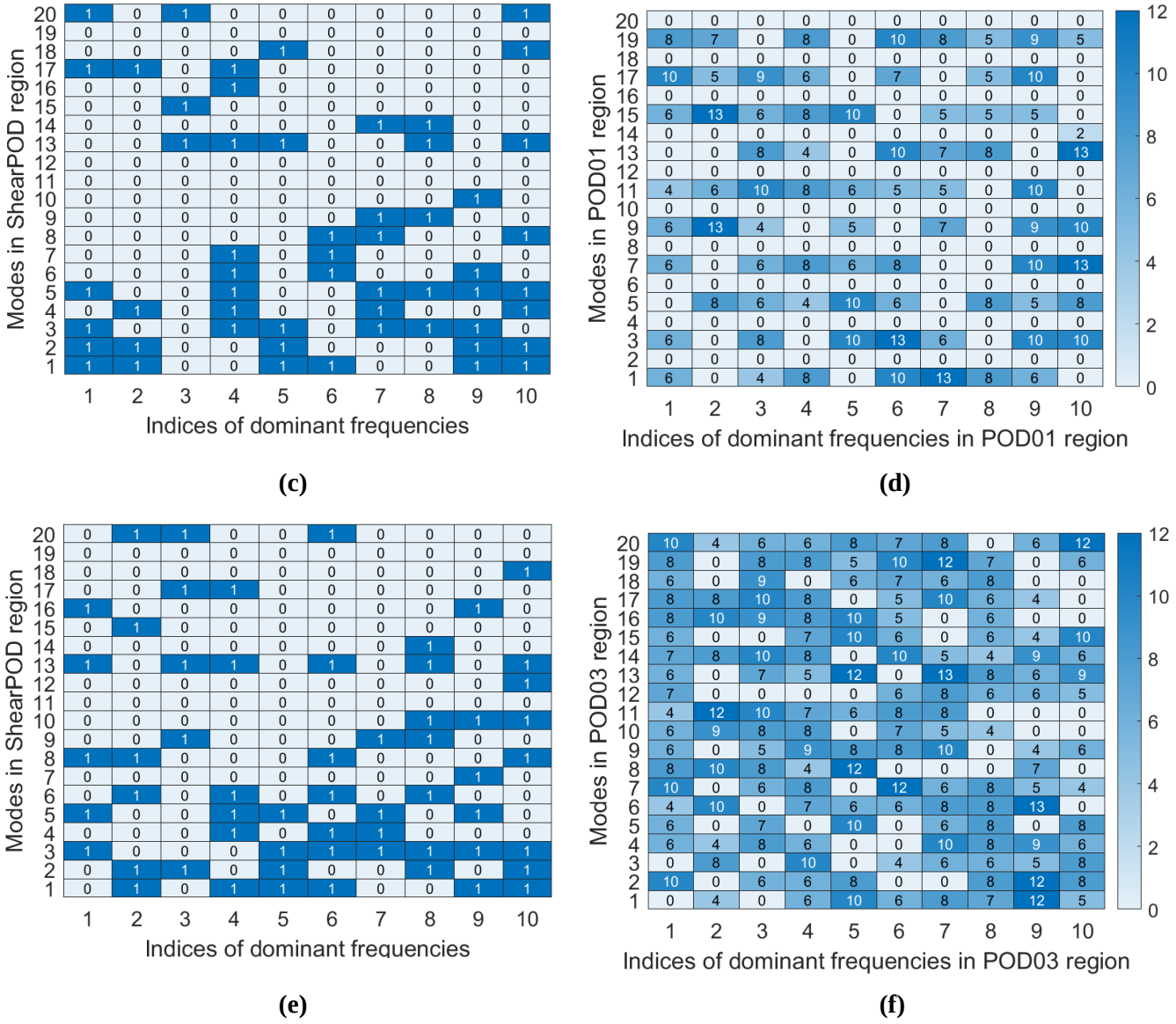

Figure 13. Heatmap of dominant frequencies interaction in POD01, POD02 and POD03 zones inside the porous region with the 20 initial modes in ShearPOD zone in the non-porous region; **Left**: Dominate frequencies interaction between mode 1 of **(a)** POD01, **(c)** POD02 and **(e)** POD03 and 20 initial modes in ShearPOD zone; Non-zero values shows the presence of dominate frequencies interaction and zero values shows no interaction between the modes; **Right**: Dominate frequencies interaction between 20 initial modes of **(b)** POD01, **(d)** POD02 and **(f)** POD03 zones and the 20 initial modes in ShearPOD zone; The numbers in the heatmap show the total co-occurrence of all the initial 20 modes in POD01, POD02, and POD03 zones with all 20 initial modes in the ShearPOD zone.

3.3 Spectral analysis

Figure 14 illustrates the power spectrum density (PSD) of the vertical velocity at various sampling points within the porous block and on the porous-fluid interface. PSD_v exhibit dominant Strouhal numbers based on ligament diameter ($St_d = f \times d \times \varepsilon / U_{in}$ where "f" is dominant frequency, "d" is mean ligament

diameter and "ε" is porosity) in the pore flow. Specifically, it shows two dominant frequencies at $St_{d,1}$ = 0.009 and $St_{d,2}$ = 0.02, at Probes #1 (at x/h = 1.22 and y/h = 0.76) and #10 (at x/h = 2.03 and y/h = 0.88) within the porous region on the positive flow leakage trajectory paths. Although the dominant frequencies in the spectral analysis of the streamwise velocity components (not shown here) exhibit similar behaviour, they differ from the dominant frequencies of the vertical velocity.

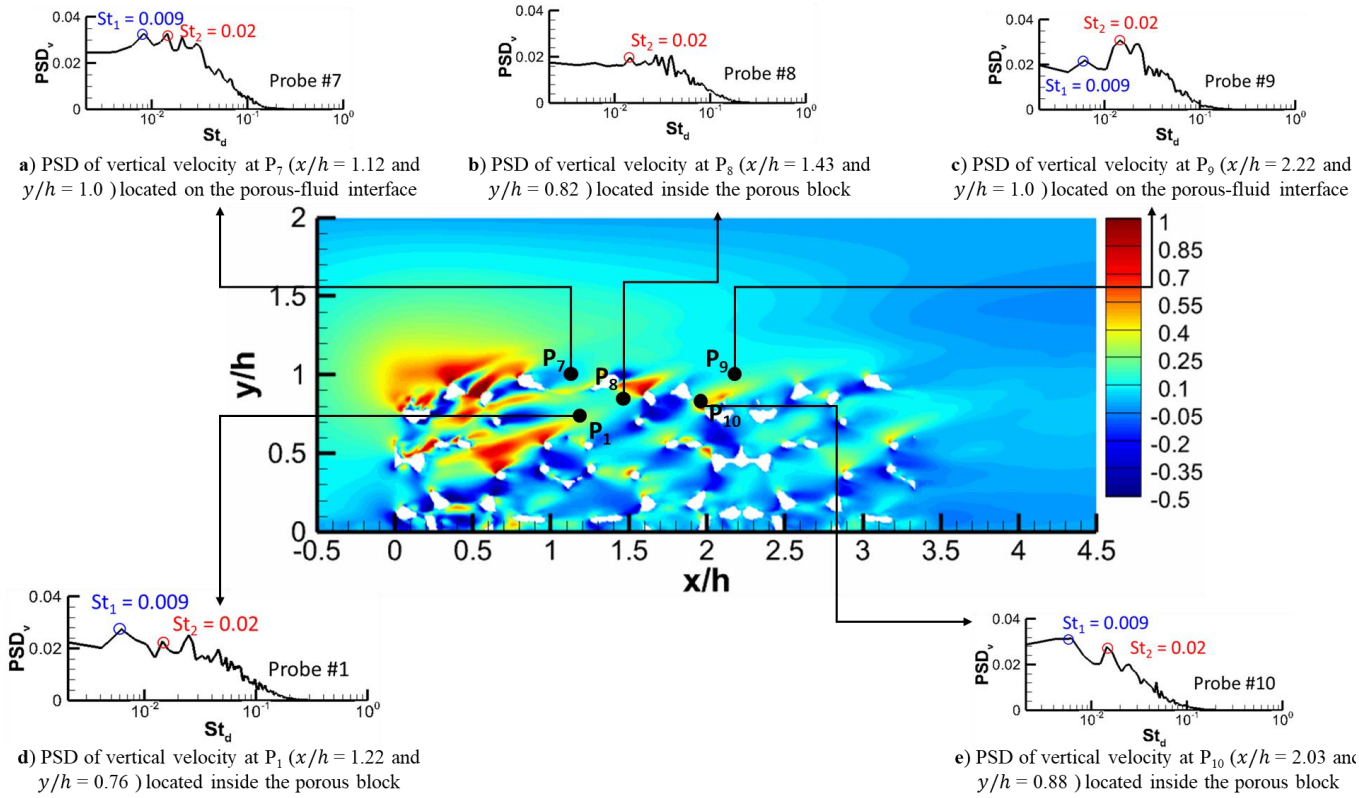

Figure 14. The contour of non-dimensional time-averaged vertical velocity ($\langle\bar{v}\rangle/U_{in}$) and its Power Spectrum Density (PSD) at different sampling points on the symmetry plane ($z/h = 0$) at Re_h = 7200 for the low porosity (ε = 85%) case.

To investigate the similarities among signals obtained from different probes, cross-correlation analysis is employed [49]. The cross-correlation coefficient $r(\tau)$, calculated using the formula ($r(\tau) = \sum_i[(\Lambda(i) - \bar{\Lambda}) \times (\Xi(i-\tau) - \bar{\Xi})] \,/\, \sqrt{\sum_i(\Lambda(i) - \bar{\Lambda})^2}\sqrt{\sum_i(\Xi(i) - \bar{\Xi})^2}$) allowed for the examination of the alignment and degree of similarity or dissimilarity between the streamwise or vertical fluctuations. The closer the cross-correlation coefficient is to 1, the stronger the relationship between the two signals (i.e., Λ and Ξ). The findings demonstrate that probes located along the flow leakage trajectory exhibit a notably high cross-correlation with a time lag (τ). For example, **Figure 15(a)** shows that the cross-correlation of streamwise fluctuations

between probes #1 and #8 has a strong correlation ($r(\tau) = 0.49$) and a time lag of $\tau = 14.8$. Conversely, for signals obtained from probes not situated along the flow leakage trajectory, the cross-correlation is comparatively weaker, as shown in **Figure 15(b)** for probes #1 and #9. This observation underscores the significant influence of flow leakage on information transfer dynamics through the porous medium

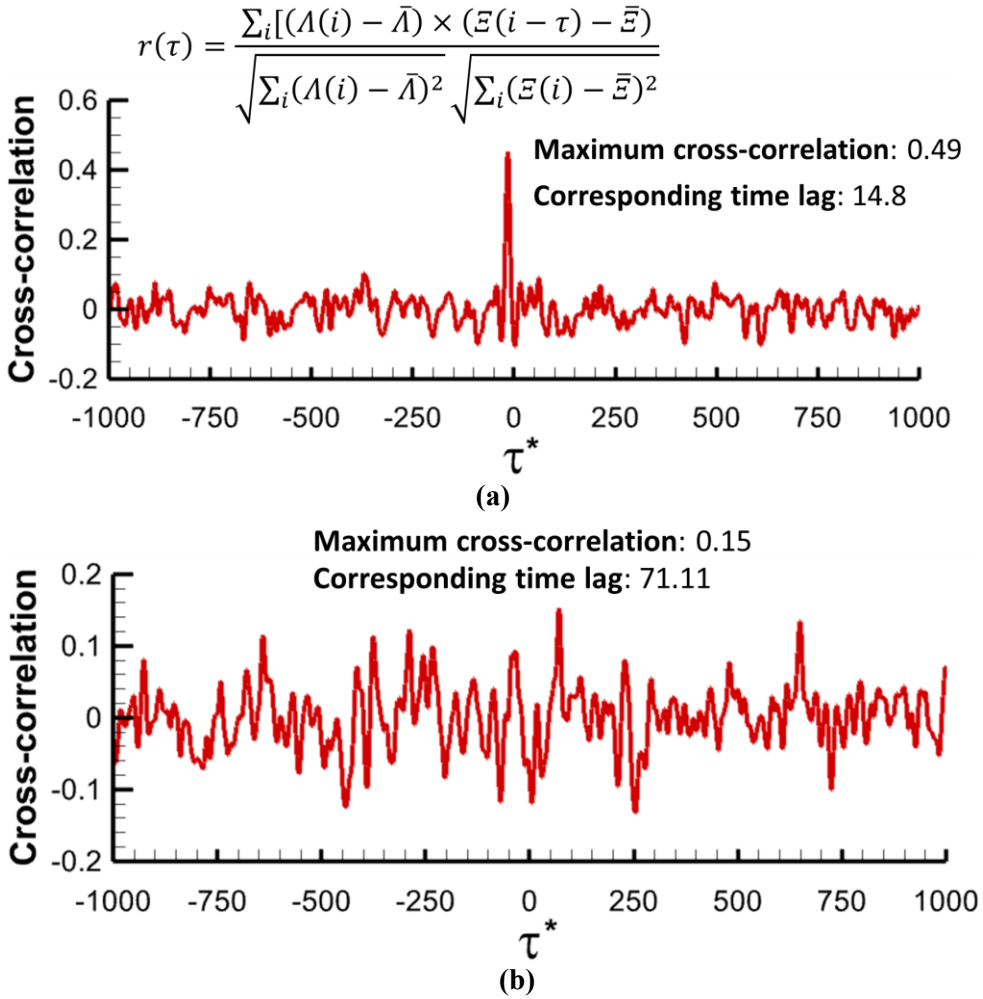

Figure 15. Cross-correlation of streamwise fluctuations between; **(a)** strong cross-correlation between probes #1 and #8, which are located along the flow leakage trajectory and **(b)** weak cross-correlation between probes #1 and #9, which are not located along the flow leakage trajectory in **Figure 14**; Strong cross-correlation suggests that flow leakage has a significant impact on the dynamics of information transfer through the porous medium.

To further investigate the time-dependent nature of the flow, the pattern of Reynolds stresses is explored. The distribution of Reynolds shear stress inside the porous region is shown in **Figure 16(a)**. The observed positive and negative patterns of Reynolds shear stress in the wake of the porous ligaments are similar to the vortex shedding phenomenon found in the wake region of a bluff body [50], which confirms the time-dependent nature of the pore flow. The flow characteristics around the porous ligaments are dependent on

various factors, including the gap ratio (G/d) of two consecutive porous ligaments, flow approaching angle (α), and local Reynolds number ($Re_{d,local} = u_{local}d/\upsilon$), where u_{local} and "υ" represent the local velocity perpendicular to the porous ligaments and the kinematic viscosity of the fluid, respectively. For very small gaps, the two ligaments may act as a single bluff body, resulting in two peaks in the Reynolds stress contours behind the downstream ligament caused by vortex shedding (zone B in **Figure 16**). Conversely, the recirculation bubbles in the gap between the ligaments exhibit minimal Reynolds stress, indicating quasi-steady flow (extended-body regime). However, if the gap between the ligaments is sufficiently large, they may behave as two independent bluff bodies (zone C in **Figure 16**), leading to the generation of Reynolds stress from alternate vortex shedding originating from the upstream ligament (co-shedding regime). **Figure 16(b)** illustrates instantaneous spanwise vorticity contours, revealing the presence of vortices within the porous region that can significantly impact information transfer dynamics. Specifically, at low gap ratios (zone B), vortex shedding only occurs in the wake of the downstream ligament, whereas at higher gap ratios (zone C), the separated shear layer from the upstream ligament rolls up to form vortices that interact with the downstream ligament, resulting in shedding both behind the downstream ligament and in the gap between the ligaments. These observations are consistent with the three major regimes based on the gap ratio: the solo-shedding, extended-body, and co-shedding regimes [51], corresponding to zones A, B, and C in **Figure 16**, respectively. These observations align with previous research by Blois et al. [25], who conducted particle image velocimetry measurements in a cubically packed bed of uniform spheres and monitored the evolution of small-scale vortices across the pore space. Their study revealed that the instantaneous flow structures within the pore space are dominated by jet flows that generate turbulent eddies. These jet flows can be horizontal, vertical, or a combination of both, with the temporal evolution of the pore flow being a function of the intensity, direction, and duration of these jets. They observed that flow characteristics in the pore space are caused by the pulsating nature of the pore flow.

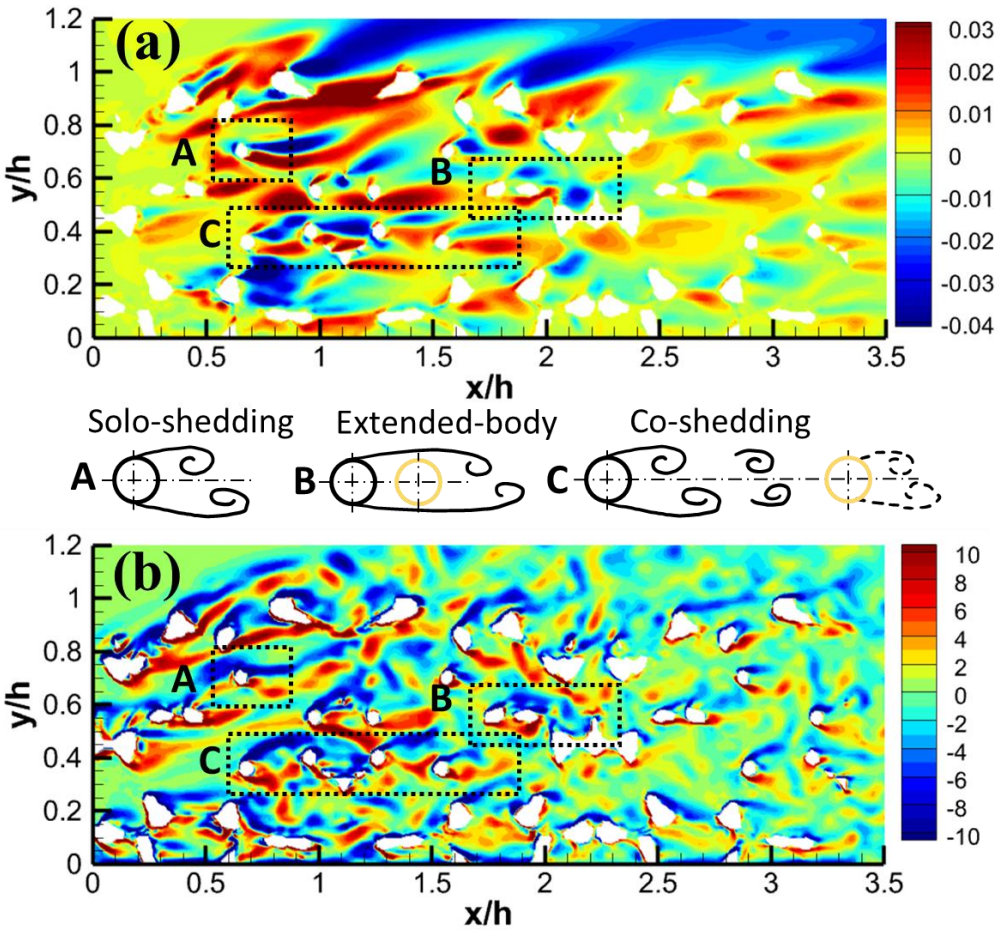

Figure 16. (a) Non-dimensional Reynolds shear stress ($\langle\overline{u'^*v'^*}\rangle = \overline{\langle u'v'\rangle} / U_{in}^2$); **(b)** spanwise vorticity ($\omega_z^* = \omega_z^* \times U_{in}/h$) inside the porous region at Re_h = 7200.

3.4 Dynamics of momentum and energy exchanges

To further investigate the physics behind the momentum exchange across the porous-fluid interface and quantify the correlations between the porous and non-porous regions, the quadrant analysis using joint probability density function (JPDF) [52] and Pearson linear correlation coefficient [53] is employed. The quadrant analysis divides the data into four quadrants based on the sign of the streamwise (u') and vertical (v') velocity fluctuations. The first quadrant (Q1) corresponds to $u' > 0$, $v' > 0$, representing outward intersection events. The second quadrant (Q2) is associated with $u' < 0$, $v' > 0$, representing ejection events. The third quadrant (Q3) corresponds to $u' < 0$, $v' < 0$, indicating inward intersection events. Lastly, the fourth quadrant (Q4) with $u' > 0$, $v' < 0$ is known as a sweep event. These distinct events have unique fluid transport characteristics, where ejection events transport low-momentum fluid upwards, sweep events transport high-momentum fluid downwards, and outward intersection events transport high-momentum fluid upwards. By utilizing the quadrant analysis and Pearson linear correlation coefficient, a comprehensive

understanding of the momentum exchange and transport processes between the porous and non-porous regions can be achieved.

Figure 17 shows the contours of the joint probability density function (JPDF) of non-dimensional velocity fluctuations, $\sigma_u = u'/u_{RMS}$ and $\sigma_v = v'/v_{RMS}$ at different sampling points inside the porous region and on the interface [52]. The Pearson linear correlation coefficient, Υ, is displayed on each subplot of **Figure 17** following [53]. The distribution of fluctuating velocities in **Figure 17** changes concerning the location of the sample point in the porous region and on the interface. The contour of JPDF on the positive flow leakage trajectory paths inside the porous block and on the porous-fluid interface illustrates an elliptical shape along $\sigma_u = \sigma_v$ with positive Υ in **Figure 17(a-c)**. This means that on the positive flow leakage trajectory paths, outward/inward intersection events are dominant. However, due to the positive mean flow leakage, there is a strong tendency for outward motion $(+v')$ of the high-momentum streamwise-oriented flow $(+u')$ from the porous region into the non-porous region (Q1 event). Furthermore, at the beginning of the porous block due to the stronger positive flow leakage, Υ is higher than that at the end of the porous block, which is consistent with previous findings in **Table 2**. Inward intersection events (Q3 events) at these sampling points are related to the pulsating nature of the positive flow leakage when the instantaneous magnitude of positive flow leakage is less than the mean value of the positive flow leakage. The trend of the JPDF in **Figure 17(a-c)**, demonstrates that, at these sampling points, information exchange is dominated by turbulent fluctuations induced by the positive flow leakage from the porous region into the non-porous region, both in terms of frequency and intensity.

At the end of the porous block on the porous-fluid interface, where the positive flow leakage is negligible, the distributions of the JPDF in **Figure 17(d)** are oval-shaped and elongated along the second and fourth quadrants (along $\sigma_u = -\sigma_v$). It is due to the ejection flow $(+v')$ across the porous-fluid interface that causes a momentum reduction $(-u')$, and wall-normal perturbation by the sweep event $(-v')$ which transports the momentum from the non-porous region to the porous region which is consistent with previous findings for fully-developed porous channel flows [17]. At this region, both ejection and sweep events are likely to occur with nearly the same intensity and frequency. Therefore, it can be concluded that at the end of the porous block, where the positive flow leakage is negligible, the information transfer by turbulent fluctuations from the porous to the non-porous region and vice versa is controlled by ejection and sweep, respectively.

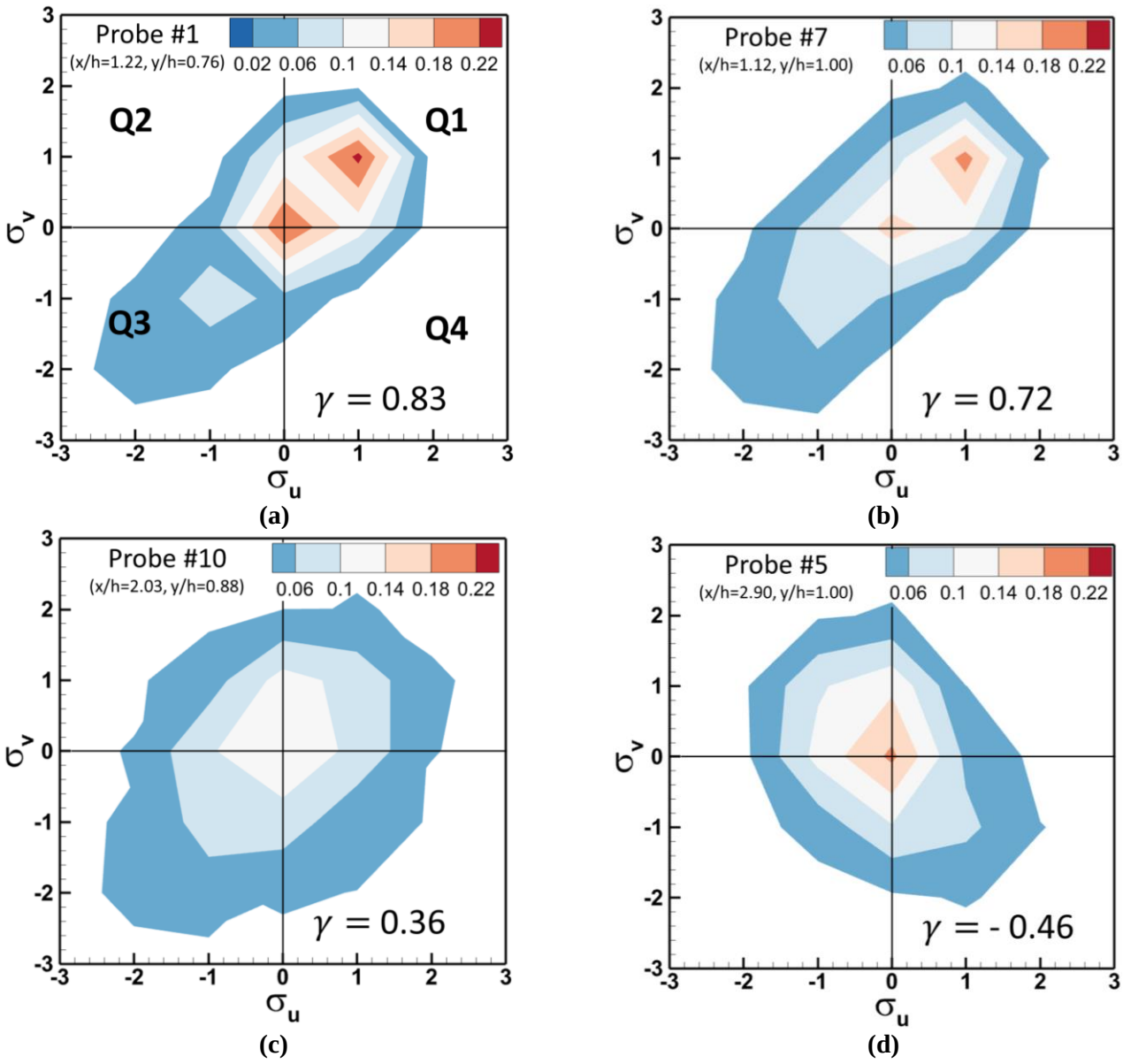

Figure 17. Contours of JPDF of $\sigma_u = u'/u_{RMS}$ and $\sigma_v = v'/v_{RMS}$ at Re_h = 7200; Probes #1, #7 and #10 are located on the positive flow leakage trajectory paths, whereas Probe #5 is located at the end of the porous block with negligible positive flow leakage; The colour scale indicates the percentage of points contained within each bin of the joint PDF. **(a)** Probe #1 inside the porous block where there is strong positive flow leakage; **(b)** Probe #7 on the porous-fluid interface where there is strong positive flow leakage; **(c)** Probe #10 inside the porous block where there is no strong positive flow leakage; **(d)** Probe #5 on the porous-fluid interface with negligible positive flow leakage.

3.5 Heat transfer

Figure 18 shows the contours of instantaneous temperature ($\overline{\Theta}$), time-averaged vertical turbulent heat flux ($\langle\overline{v'^{*}\theta}\rangle$) and time-averaged convective heat fluxes in the streamwise ($\langle\bar{u}\overline{\mathbb{T}}\rangle$) and vertical ($\langle\bar{v}\overline{\mathbb{T}}\rangle$) directions. for both high and low porosity. The convective heat fluxes show heat transfer by the mean streamwise, and

vertical flow presented in **Figure 5**, which predominantly showcases upward and forward flow within the POD01 zone. Turbulent heat flux corresponds to the turbulence fluctuations induced by spatial modes discussed in **Figure 10** and **Figure 11**.

Figure 18(a-b) shows that after the flow impingement on the windward face of the porous blocks, the low-temperature flow penetrates the pores of the porous block and forms high-momentum channelling in the porous region. Contours for $\overline{v'^*\theta}$, which is a measure of the vertical (wall normal) turbulent transport of thermal energy, are shown in **Figure 18(c-d)**. The complex patterns of $\overline{v'^*\theta}$ with positive and negative values challenges the predictable notion of heat transfer by unidirectional flow within porous materials discussed in **Figure 5**. However, at the beginning of the porous region ($0 \leq x/h \leq 1.0$) , these contours show that $\langle\overline{v'^*\theta}\rangle$ is generally negative on the trajectory path of the positive flow leakage (see also **Figure 5**). This is consistent with positive flow leakage of low-temperature fluid towards the non-porous region. The local peak values of $\langle\overline{v'^*\theta}\rangle \leq$ -0.005 are in the regions where there is strong positive flow leakage (see **Figure 5(c)**). The location of peak levels of $\langle\overline{v'^*\theta}\rangle$ are consistent with the peak values for $\langle\overline{u'^*v'^*}\rangle$ that indicates the high-momentum positive flow leakage of low-temperature fluid flow. In the end section of the porous region ($2.0 \leq x/h \leq 3.0$) there is no clear trend for the $\langle\overline{v'^*\theta}\rangle$ that means information transfer by turbulent fluctuations across a spectrum of directions.

High positive values of vertical convective heat flux in **Figure 18(e-f)** prove the flow leakage of low-temperature high-momentum flows from the porous region. Contours of time-averaged streamwise convective heat flux in **Figure 18(g-h)** confirm the previous discussion regarding the momentum exchange between porous and non-porous regions by the flow leakage and channelling effect. High values of streamwise convective flux in **Figure 18(g)** show that high-momentum flow from the porous region leaks to the non-porous region and consequently transfers low-temperature flow that has entered the porous region from the leading surface to the non-porous region. **Figure 18(h)** shows the convection of high-momentum low-temperature flows inside the porous block due to the channelling effect for the high porosity case.

This observation corroborates our prior discussions, emphasizing the pivotal role of the mean flow (Mode 0) as the primary medium for information transfer. It facilitates convective heat transfer from the porous to the non-porous region through upward and forward flow movements. Furthermore, the turbulent heat flux inherent in alternate POD modes (Mode $\neq$ 0) significantly contributes to information propagation in diverse directions. Notably, during the initial phase of the porous block, a distinctive occurrence of high negative values in turbulent heat flux is observed, attributed to the trajectory of flow leakage.

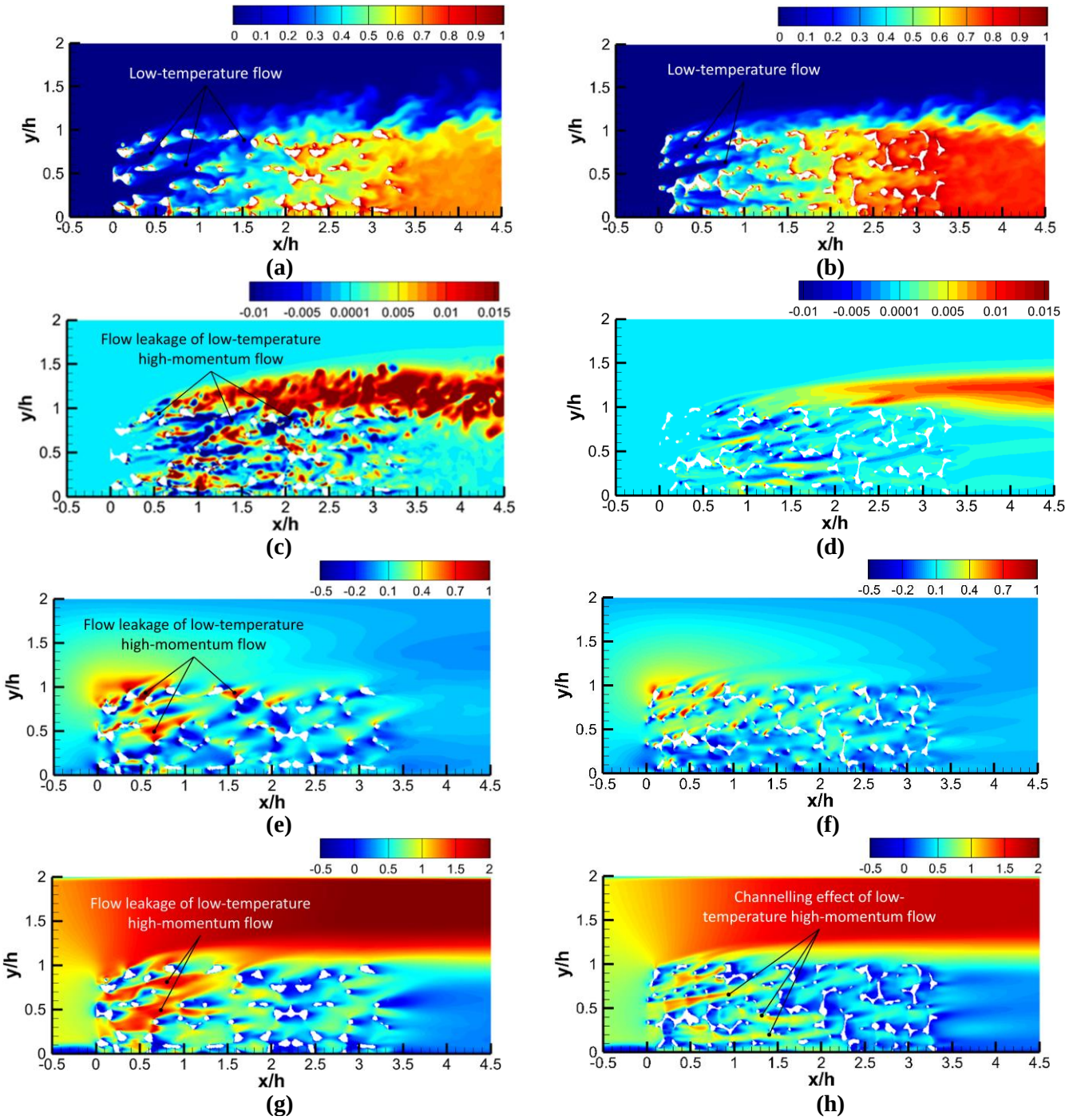

Figure 18. First row: Non-dimensional instantaneous temperature ($\overline{\Theta} = \frac{\overline{T-T_{in}}}{T_s-T_{in}}$); **Second row**: Time-averaged vertical turbulent heat flux ($\langle\overline{v'^*\theta}\rangle = \langle\overline{\frac{v'}{U_{in}} \times \frac{T'}{T_s-T_{in}}}\rangle$) contours; **Third row**: Time-averaged vertical convective heat flux ($\langle\bar{v}\overline{\mathbb{T}}\rangle = \langle\overline{\frac{v}{U_{in}}} \times \overline{\frac{T}{T_s-T_{in}}}\rangle$); **Forth row**: Time-averaged streamwise convective heat flux ($\langle\bar{u}\overline{\mathbb{T}}\rangle = \langle\overline{\frac{u}{U_{in}}} \times \overline{\frac{T}{T_s-T_{in}}}\rangle$) at symmetry plane ($z/h = 0$) for Re_h = 7200. **Left**: Low porosity; **Right**: High porosity.

Figure 19(a, c) provides a comprehensive 3D depiction of the time-averaged Nusselt number ($\langle Nu \rangle$) corresponding to the mean flow (Mode=0) discussed in **Figure 5**. The impingement of the low-temperature, high-momentum flow stream to the windward face of the porous blocks leads to the peak values of Nusselt number in the stagnation region for all cases. The Nu magnitude consistently reduces as the flow traverses the metal foam, reaching its lowest point at the trailing edge of the metal foam. This decline is attributed to the diminishing temperature difference between the ligaments and the surrounding flow, coupled with a reduction in mass flow rates at each section of the porous block due to flow leakage. Notably, the figure highlights a substantial portion of the porous ligaments experience insufficient cooling, particularly in the downstream region for both cases. **Figure 19(b, d)** presents a 3D visualization illustrating the Fluctuation of Nusselt number (Nu') in correlation with distinct flow structures (Mode ≠ 0) as previously discussed in **Figure 11**. The observation of both negative and positive Nusselt numbers at various spatial positions reflects the intricate turbulent fluctuations inherent in POD modes (Mode ≠ 0), particularly exemplified by modes 1 and 6 in **Figure 11**. These fluctuations play a pivotal role in facilitating turbulent heat transfer across a diverse spectrum of directions inside the porous region and across the porous-fluid interface. Notably, in comparison to the average Nusselt number $\langle Nu \rangle$, elevated values of Nu' are discernible at various locations within the porous block, underscoring the critical influence of turbulent spatial structures in modulating momentum exchange dynamics and heat transfer within the stochastic metal foam.

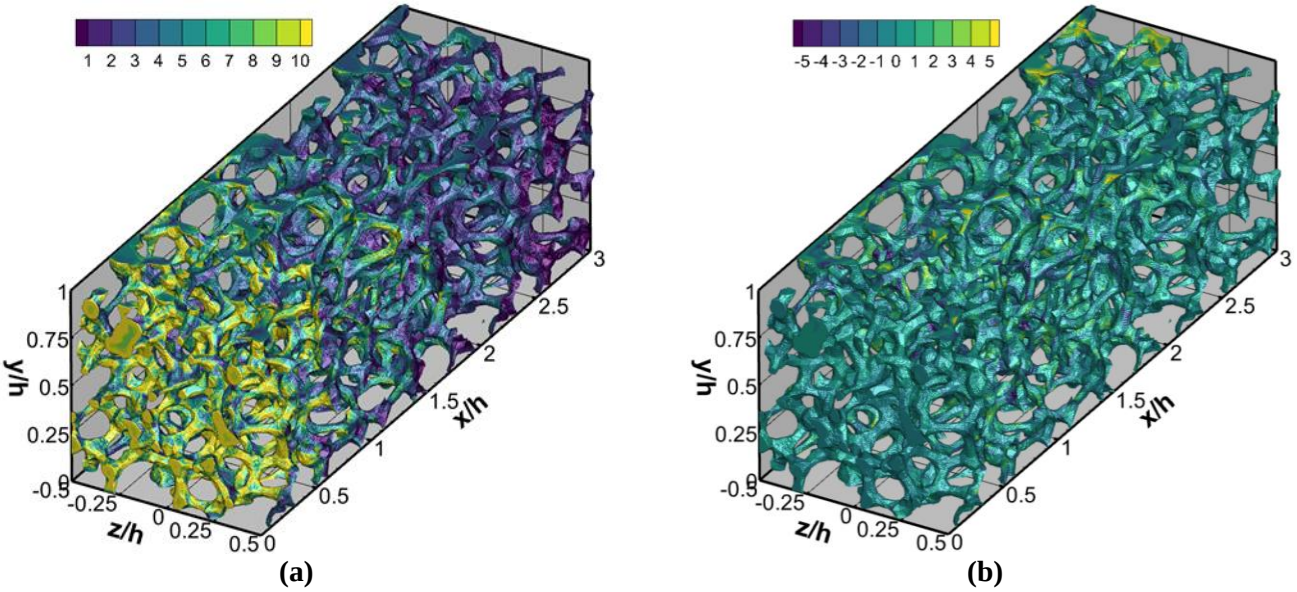

(a) **(b)**

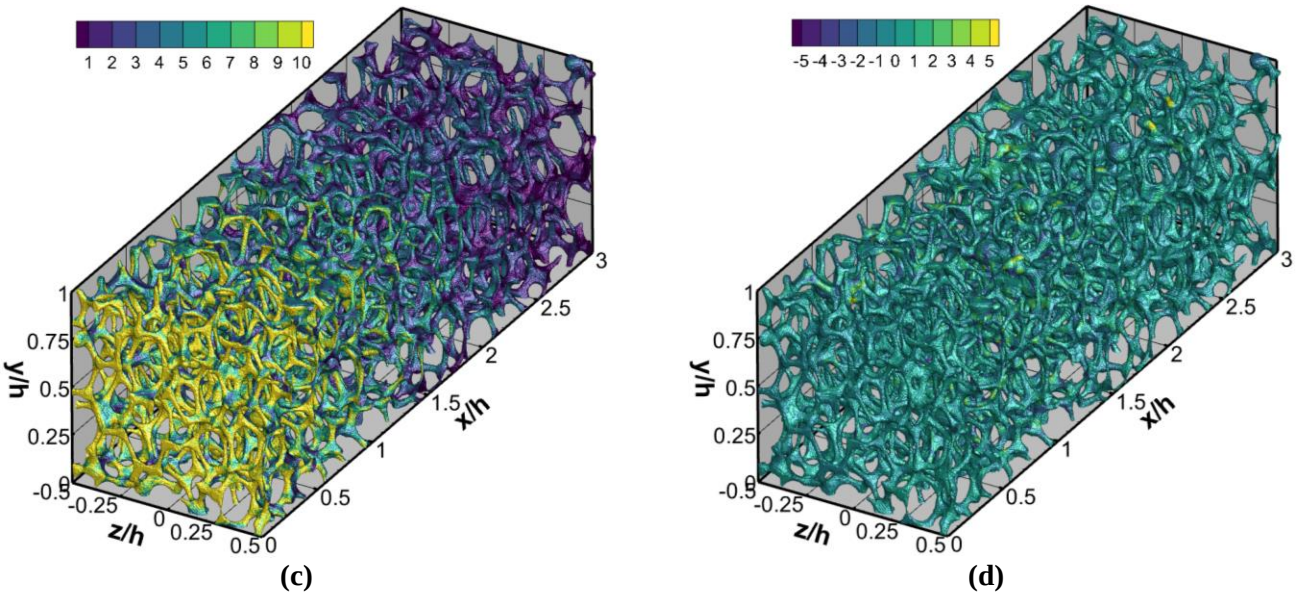

Figure 19. Three-dimensional distribution of **left**: time-averaged Nusselt number ($\langle Nu \rangle = \langle h_c \rangle \, h/k_f$); **Right**: Fluctuation of Nusselt number ($Nu' = (h_c - \langle h_c \rangle) \, h/k_f$) at Re_h = 7200. **(a-b)** Low porosity (ε = 85%); **(c-d)** High porosity (ε = 91%).

The streamwise distribution of the normalized Nusselt number ($Nu/\, Nu_o$) for all cases is depicted in **Figure 20(a)**. Normalization is based on Nu_o ($Nu_o = \int_{-0.65h}^{0.65h} \int_0^{3h} Nu dx dz$), representing the average Nu value at Re_h = 7200 for the low porosity case. The figure illustrates a direct correlation between porosity and Nu values; higher porosity corresponds to elevated Nu numbers for all cases. For instance, at Re_h = 7200 and Re_h = 1800, the average Nu values for the high porosity case are 20% and 18% higher than those for the low porosity cases, respectively. This trend aligns with the flow leakage values presented in **Table 2**, confirming that higher porosity cases exhibit lower flow leakage.

Furthermore, the figure reveals that over 60% of the averaged Nusselt numbers for all cases are achieved within the initial third of the porous block length ($0 \leq x/h \leq 1.0$), as previously demonstrated in **Figure 14**. At lower Reynolds numbers, characterized by reduced flow momentum, the penetration length of the channelling effect is diminished compared to higher Reynolds cases. This phenomenon is visible in the end section of the porous block ($1.8 \leq$ x/h ≤ 3.0), where Nusselt numbers exhibit relative constancy, and heat transfer between the porous block and pore flows is negligibly affected. However, in cases with higher Reynolds numbers, the distribution of Nu numbers at the end section of the porous block between $1.8 \leq x/h \leq 3.0$ is not as uniform as in the low Re case. This discrepancy is attributed to the greater penetration of low-temperature flow into the porous structure and reduced flow leakage at higher Reynolds numbers, as detailed in **Table 2** and **Figure 18**.

Moreover, the Root mean square (RMS) of the Nusselt number (Nu_{RMS}) in **Figure 20(b)** shows two different trends for low and high Re numbers. At high Re number the maximum Nu_{RMS} occurs in the first half of the porous block and the second part of the porous block the Nu_{RMS} is nearly constant around 0.027. the trends of Nu_{RMS} at high Re number is consistent with the turbulence fluctuation discussed in **Figure 18** where at the first half of the porous block higher values of turbulence fluctuation exits. However, at the low Re number the trend of the Nu_{RMS} is different. In the second half the porous block has high values of Nu_{RMS} happens that means at the beginning of the porous block the fluctuation of heat transfer from the porous ligament is negligible and in the second half of the porous block Nu_{RMS} increases because of the low values of the $\langle Nu \rangle$ at this region.

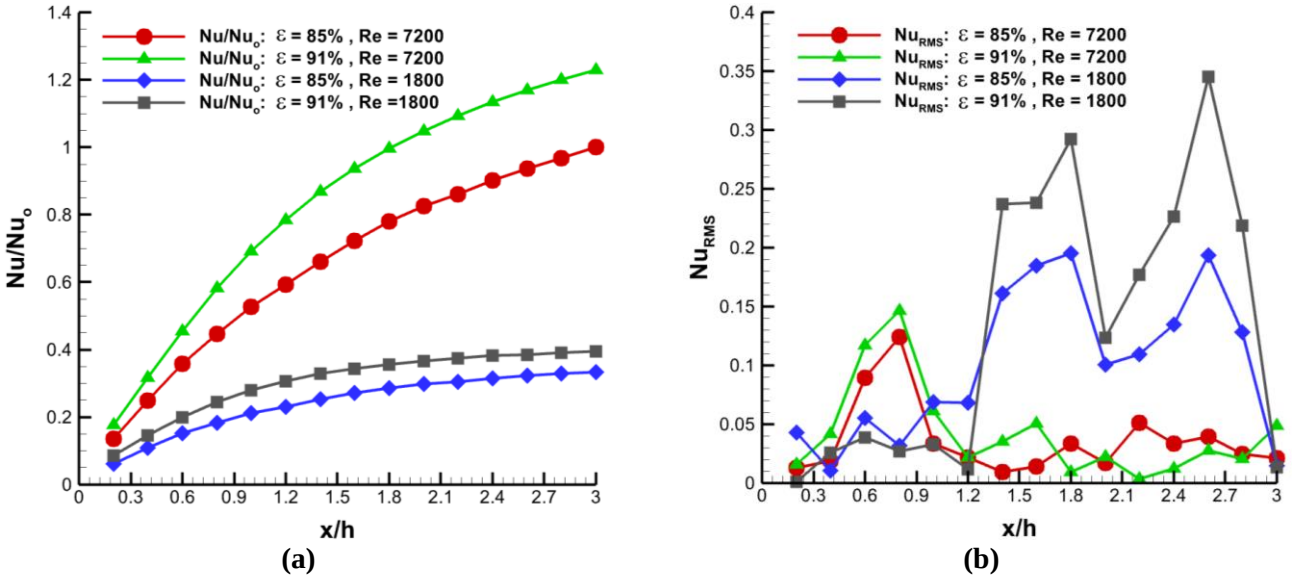

Figure 20. (a) Streamwise distribution of the normalized Nusselt number ($Nu/\ Nu_o$) for all cases. The base Nusselt number, Nu_o ($Nu_o = \int_{-0.65h}^{0.65h}\int_0^{3h} Nudxdz$), correspond to the average Nu value at Re_h = 7200 for the low porosity case; **(b)** Root mean square (RMS) of Nusselt number ($Nu_{RMS} = \frac{1}{\langle Nu \rangle}\sqrt{(Nu - \langle Nu \rangle)^2}$) for all cases.

The Root Mean Square (RMS) of the Nusselt number (Nu_{RMS}) depicted in **Figure 20(b)** exhibits distinct behaviours at varying Reynolds numbers. Specifically, at high Reynolds numbers, Nu_{RMS} peaks in the initial half of the porous block, maintaining a relatively constant value of approximately 0.027 in the latter half. This observed Nu_{RMS} pattern at high Reynolds numbers aligns with the turbulence fluctuations detailed in **Figure 18**, where heightened turbulence fluctuation is evident in the first half of the porous block. Conversely, at low Reynolds numbers, a contrasting trend emerges. At low Re, elevated Nu_{RMS} values are observed in the latter half of the porous block, indicating minimal heat transfer fluctuations from the porous

ligament at the porous block's onset. Subsequently, Nu_{RMS} increases towards the end of the porous block due to the decrease in average Nusselt numbers ($\langle Nu \rangle$) in this region, rather than an increase in fluctuations. Due to the stochastic nature of the porous ligament, the distribution of Nu_{RMS} is not smooth, even though the sampling time for the time-averaging period is sufficiently high, as elucidated in **Table 1**.

4 Conclusions

This study underscores the critical importance of investigating information transfer at the pore scale within composite porous-fluid systems characterized by stochastic pore distribution. Prior research has highlighted contrasting behaviours in turbulent momentum exchange and heat transfer between finite porous blocks in turbulent channel flow and fully developed channel flow. In addition, a significant gap persists in our understanding, due to the prevalent focus on simplified porous structures like smoothed cubes or spheres. This study addresses this deficiency and fills the gap by employing high-fidelity pore-scale Large Eddy Simulations (LES) to explore the intricate dynamics of momentum exchange and heat transfer across the porous-fluid interface. By introducing a novel methodology based on data-driven modal analysis, including Proper Orthogonal Decomposition (POD) and time–frequency analysis, this research pioneers a comprehensive examination of the interactions between porous and non-porous regions. The insights gained from this investigation shed light on the interplay of convective and turbulent fluxes, revealing their collective impact on heat transfer within composite porous-fluid systems. This study unveils the nuanced time-dependent mechanisms that govern information exchange in complex porous media environments, marking a significant advancement in our understanding of these systems. The findings of this study can be summarized as follows:

1. Flow visualization employing Proper Orthogonal Decomposition (POD) spatial structures for distinct modes establishes a robust connection between the fluid dynamics within the porous region and the vertical transport of fluid across the permeable porous-fluid interface situated in the porous domain. The comprehensive analysis discerns both positive and negative flow leakage phenomena. Specifically, positive flow leakage from the porous region into the non-porous region exhibits a predominant occurrence within the initial segment of the porous block ($0 \leq x/h \leq 1.0$), predominantly governed by mode = 0, representing the mean flow. Contrarily, negative flow leakage, denoting local flow penetration from the non-porous to the porous region, is anticipated in the wake of porous ligaments at the interface for all modes, underscoring the multi-modal nature of the observed fluid dynamics in the composite porous-fluid system.

2. Spatial structures across various POD modes disclose the paramount significance of the mean flow (Mode = 0) as the principal driver of momentum exchange and heat transfer. This mode governs convective heat transfer from the porous to the non-porous region through both upward and forward flow movements, distinctly manifesting as positive flow leakage. Moreover, the interplay of turbulent heat flux within alternate POD modes (Mode ≠ 0) enhances the propagation of thermal information in diverse directions, thereby adding a nuanced layer to the complexity of the observed heat transfer dynamics. This exploration underscores the pivotal role of different POD modes in explaining the multifaceted mechanisms governing momentum and heat transport in composite-porous fluid systems.

3. The spectral analysis of temporal modes exposes the dynamic interplay between flow structures in the porous and non-porous regions. The exploration of mode interaction shows compelling insights, particularly in the initial segment of the porous block (POD01 zone), where the occurrence of positive flow leakage is observed. In this zone, an increase in dominant frequency interaction values, indicating elevated dynamism in the information transport is predicted. In contrast, as one progresses towards the middle (POD02 zone) and concluding sections (POD03 zone) of the porous region, a reduction in dominant frequency interaction is evident.

4. Conducting a quadrant analysis on turbulence fluctuations through the utilization of the joint probability density function unveils compelling insights. In regions characterized by robust positive flow leakage, a dynamic exchange of information is discerned, facilitated by both outward and inward interactions. In contrast, where positive flow leakage is minimal, the information transfer mechanisms predominantly hinge upon ejection and sweep events.

5. Examining the streamwise distribution of the Nusselt number reveals a discernible trend wherein the magnitude of the Nusselt number consistently diminishes as the flow progresses through the metal foam, reaching its apogee at the trailing edge of the material. This reduction is ascribed to the dwindling temperature gradient between the ligaments and the surrounding flow, coupled with a concurrent decrease in mass flow rates at each segment of the porous block attributable to flow leakage. The findings underscore a significant observation: over 60% of the averaged Nusselt numbers across all cases are attained within the initial third of the porous block length ($0 \leq x/h \leq 1.0$), emphasizing the pivotal role of the initial section in governing heat transfer characteristics within the porous medium.

Acknowledgement

This work was supported by the UK Engineering and Physical Sciences Research Council (EPSRC) [grant numbers EP/W033542/1]. This work used the ARCHER2 UK National Supercomputing Service (https://www.archer2.ac.uk).

References:

[1] W. Q. Li, Y. X. Li, T. H. Yang, T. Y. Zhang, and F. Qin, "Experimental investigation on passive cooling, thermal storage and thermoelectric harvest with heat pipe-assisted PCM-embedded metal foam," *International Journal of Heat and Mass Transfer,* vol. 201, p. 123651, 2023/02/01/ 2023, doi: https://doi.org/10.1016/j.ijheatmasstransfer.2022.123651.

[2] Z. Zhang *et al.*, "Pore-scale simulation of forced convection heat transfer in metal foams with uniform and gradient structures," *Applied Thermal Engineering,* vol. 225, p. 120074, 2023/05/05/ 2023, doi: https://doi.org/10.1016/j.applthermaleng.2023.120074.

[3] H. Rho, Y. S. Jang, H. Bae, A.-N. Cha, S. H. Lee, and J.-S. Ha, "Fanless, porous graphene-copper composite heat sink for micro devices," *Scientific Reports,* vol. 11, no. 1, p. 17607, 2021/09/02 2021, doi: 10.1038/s41598-021-97165-y.

[4] Z. Sun *et al.*, "Experimental study of battery passive thermal management system using copper foam-based phase change materials," *International Journal of Thermofluids,* vol. 17, p. 100255, 2023/02/01/ 2023, doi: https://doi.org/10.1016/j.ijft.2022.100255.

[5] Z. Fan, Y. Fu, R. Gao, and S. Liu, "Investigation on heat transfer enhancement of phase change material for battery thermal energy storage system based on composite triply periodic minimal surface," *Journal of Energy Storage,* vol. 57, p. 106222, 2023/01/01/ 2023, doi: https://doi.org/10.1016/j.est.2022.106222.

[6] A. Manthiram and A. Bhargav, "Less pore equals more," *Nature Energy,* vol. 4, no. 11, pp. 908-909, 2019/11/01 2019, doi: 10.1038/s41560-019-0495-y.

[7] G. K. Marri and C. Balaji, "Experimental and numerical investigations on the effect of porosity and PPI gradients of metal foams on the thermal performance of a composite phase change material heat sink," *International Journal of Heat and Mass Transfer,* vol. 164, p. 120454, 2021/01/01/ 2021, doi: https://doi.org/10.1016/j.ijheatmasstransfer.2020.120454.

[8] H. Liu *et al.*, "Numerical study on the thermal performance of foam-metal composite phase change material in different force fields," *International Journal of Heat and Mass Transfer,* vol. 211, p. 124181, 2023/09/01/ 2023, doi: https://doi.org/10.1016/j.ijheatmasstransfer.2023.124181.

[9] S. Wu, Y. Chen, Z. Chen, J. Wang, M. Cai, and J. Gao, "Shape-stabilized phase change material with highly thermal conductive matrix developed by one-step pyrolysis method," *Scientific Reports,* vol. 11, no. 1, 2021, doi: 10.1038/s41598-021-80964-8.

[10] W.-J. Wang *et al.*, "Friction factor for turbulent open channel flow covered by vegetation," *Scientific Reports,* vol. 9, no. 1, p. 5178, 2019/03/26 2019, doi: 10.1038/s41598-019-41477-7.

[11] Y. Barwise and P. Kumar, "Designing vegetation barriers for urban air pollution abatement: a practical review for appropriate plant species selection," *npj Climate and Atmospheric Science*, vol. 3, no. 1, 2020, doi: 10.1038/s41612-020-0115-3.

[12] M. Jadidi, A. Revell, and Y. Mahmoudi, "Pore-scale large eddy simulation of turbulent flow and heat transfer over porous media," Applied Thermal Engineering, vol. 215, p. 118916, 2022/10/01/ 2022, doi: https://doi.org/10.1016/j.applthermaleng.2022.118916.

[13] https://www.coolingzone.com/index.php?read=648&onmag=true&type=press.

[14] M. Jadidi, H. K. Param, and Y. Mahmoudi, "On the mechanism of turbulent heat transfer in composite porous-fluid systems with finite length porous blocks: Effect of porosity and Reynolds number," International Journal of Heat and Mass Transfer, vol. 208, p. 124006, 2023/07/01/ 2023, doi: https://doi.org/10.1016/j.ijheatmasstransfer.2023.124006.

[15] M. Jadidi, H. K. Param, A. Revell, and Y. Mahmoudi, "Flow leakage and Kelvin–Helmholtz instability of turbulent flow over porous media," Physics of Fluids, vol. 34, no. 10, p. 105114, 2022, doi: 10.1063/5.0111195.

[16] K. Suga, M. Mori, and M. Kaneda, "Vortex structure of turbulence over permeable walls," *International Journal of Heat and Fluid Flow*, vol. 32, no. 3, pp. 586-595, 2011/06/01/ 2011, doi: https://doi.org/10.1016/j.ijheatfluidflow.2011.02.016.

[17] W. P. Breugem, B. J. Boersma, and R. E. Uittenbogaard, "The influence of wall permeability on turbulent channel flow," *Journal of Fluid Mechanics*, vol. 562, p. 35, 2006, doi: 10.1017/s0022112006000887.

[18] K. Suga, Y. Okazaki, and Y. Kuwata, "Characteristics of turbulent square duct flows over porous media," *Journal of Fluid Mechanics*, vol. 884, 2020, doi: 10.1017/jfm.2019.914.

[19] G. Rousseau and C. Ancey, "Scanning PIV of turbulent flows over and through rough porous beds using refractive index matching," *Experiments in Fluids*, vol. 61, no. 8, 2020-08-01 2020, doi: 10.1007/s00348-020-02990-y.

[20] Y. Kuwata and K. Suga, "Transport mechanism of interface turbulence over porous and rough walls," *Flow Turbulence and Combustion*, vol. 97, no. 4, pp. 1071-1093, 2016, doi: 10.1007/s10494-016-9759-9.

[21] T. Kim, G. Blois, J. L. Best, and K. T. Christensen, "Experimental evidence of amplitude modulation in permeable-wall turbulence," *Journal of Fluid Mechanics*, vol. 887, 2020, doi: 10.1017/jfm.2019.1027.

[22] D. Pokrajac and C. Manes, "Velocity Measurements of a Free-Surface Turbulent Flow Penetrating a Porous Medium Composed of Uniform-Size Spheres," *Transport in Porous Media*, vol. 78, no. 3, p. 367, 2009/02/07 2009, doi: 10.1007/s11242-009-9339-8.

[23] B. L. White and H. M. Nepf, "Shear instability and coherent structures in shallow flow adjacent to a porous layer," *Journal of Fluid Mechanics*, vol. 593, pp. 1-32, 2007, doi: 10.1017/s0022112007008415.

[24] C. Manes, D. Pokrajac, I. McEwan, and V. Nikora, "Turbulence structure of open channel flows over permeable and impermeable beds: A comparative study," *Physics of Fluids*, vol. 21, no. 12, 2009, doi: 10.1063/1.3276292.

[25] G. Blois, G. H. Sambrook Smith, J. L. Best, R. J. Hardy, and J. R. Lead, "Quantifying the dynamics of flow within a permeable bed using time-resolved endoscopic particle imaging velocimetry (EPIV)," *Experiments in Fluids,* vol. 53, no. 1, pp. 51-76, 2012, doi: 10.1007/s00348-011-1198-8.

[26] C. Manes, D. Pokrajac, I. Mcewan, and V. Nikora, "Turbulence structure of open channel flows over permeable and impermeable beds: A comparative study," *Physics of Fluids,* vol. 21, no. 12, p. 125109, 2009-12-01 2009, doi: 10.1063/1.3276292.

[27] X. Chu, W. Wang, G. Yang, A. Terzis, R. Helmig, and B. Weigand, "Transport of turbulence across permeable interface in a turbulent channel flow: Interface-resolved direct numerical simulation," *Transport in Porous Media,* vol. 136, no. 1, pp. 165-189, 2021-01-01 2021, doi: 10.1007/s11242-020-01506-w.

[28] T. Kim, G. Blois, J. L. Best, and K. T. Christensen, "Experimental study of turbulent flow over and within cubically packed walls of spheres: Effects of topography, permeability and wall thickness," *International Journal of Heat and Fluid Flow,* vol. 73, pp. 16-29, 2018-10-01 2018, doi: 10.1016/j.ijheatfluidflow.2018.06.004.

[29] J. J. Voermans, M. Ghisalberti, and G. N. Ivey, "The variation of flow and turbulence across the sediment–water interface," *Journal of Fluid Mechanics,* vol. 824, pp. 413-437, 2017-08-10 2017, doi: 10.1017/jfm.2017.345.

[30] S. Vollmer, F. D. L. S. Ramos, H. Daebel, and G. Kühn, "Micro scale exchange processes between surface and subsurface water," *Journal of Hydrology,* vol. 269, no. 1-2, pp. 3-10, 2002-12-01 2002, doi: 10.1016/s0022-1694(02)00190-7.

[31] X. Chu, W. Wang, G. Yang, A. Terzis, R. Helmig, and B. Weigand, "Transport of Turbulence Across Permeable Interface in a Turbulent Channel Flow: Interface-Resolved Direct Numerical Simulation," Transport in Porous Media, vol. 136, no. 1, pp. 165-189, 2021, doi: 10.1007/s11242-020-01506-w.

[32] Y. Kuwata and K. Suga, "Transport Mechanism of Interface Turbulence over Porous and Rough Walls," *Flow, Turbulence and Combustion,* vol. 97, no. 4, pp. 1071-1093, 2016, doi: 10.1007/s10494-016-9759-9.

[33] N. F. Jouybari and T. S. Lundström, "Investigation of a thin permeable layer effect on turbulent flow and passive scalar transport in a channel," *Powder Technology,* vol. 377, pp. 115-127, 2021/01/02/ 2021, doi: https://doi.org/10.1016/j.powtec.2020.08.068.

[34] F. Shikh Anuar, I. Ashtiani Abdi, and K. Hooman, "Flow visualization study of partially filled channel with aluminium foam block," *International Journal of Heat and Mass Transfer,* vol. 127, pp. 1197-1211, 2018, doi: 10.1016/j.ijheatmasstransfer.2018.07.047.

[35] J. M. Leu, H. C. Chan, and M. S. Chu, "Comparison of turbulent flow over solid and porous structures mounted on the bottom of a rectangular channel," *Flow Measurement and Instrumentation,* vol. 19, no. 6, pp. 331-337, 2008/12/01/ 2008, doi: 10.1016/j.flowmeasinst.2008.05.001.

[36] M. Jadidi, H. K. Param, A. Revell, and Y. Mahmoudi, "Flow leakage and Kelvin–Helmholtz instability of turbulent flow over porous media," *Physics of Fluids,* vol. 34, no. 10, p. 105114, 2022/10/01 2022, doi: 10.1063/5.0111195.

[37] G. Yan *et al.*, "Experimental study on flow and heat transfer performance of triply periodic minimal surface structures and their hybrid form as disturbance structure," *International Communications in Heat and Mass Transfer*, vol. 147, p. 106942, 2023/10/01/ 2023, doi: https://doi.org/10.1016/j.icheatmasstransfer.2023.106942.

[38] S. B. Pope, *Turbulent Flows*. Cambridge: Cambridge University Press, 2000.

[39] W.-W. Kim, S. Menon, W.-W. Kim, and S. Menon, "Application of the localized dynamic subgrid-scale model to turbulent wall-bounded flows," in *35th Aerospace Sciences Meeting and Exhibit*, 1997, p. 210.

[40] H. Jasak, A. Jemcov, and Z. Tukovic, "OpenFOAM: A C++ library for complex physics simulations," in *International workshop on coupled methods in numerical dynamics*, 2007, vol. 1000: IUC Dubrovnik Croatia, pp. 1-20.

[41] F. Bazdidi-Tehrani, A. Ghafouri, and M. Jadidi, "Grid resolution assessment in large eddy simulation of dispersion around an isolated cubic building," *Journal of Wind Engineering and Industrial Aerodynamics*, vol. 121, pp. 1-15, 2013/10/01/ 2013, doi: https://doi.org/10.1016/j.jweia.2013.07.003.

[42] L. Davidson, "Large Eddy Simulations: How to evaluate resolution," International Journal of Heat and Fluid Flow, vol. 30, no. 5, pp. 1016-1025, 2009, doi: 10.1016/j.ijheatfluidflow.2009.06.006.

[43] S. B. Pope, "Ten questions concerning the large-eddy simulation of turbulent flows," *New Journal of Physics*, vol. 6, no. 1, p. 35, 2004.

[44] I. Celik, M. Klein, and J. Janicka, "Assessment Measures for Engineering LES Applications," *Journal of Fluids Engineering*, vol. 131, no. 3, p. 031102, 2009-03-01 2009, doi: 10.1115/1.3059703.

[45] C. Amor, J. M. Pérez, P. Schlatter, R. Vinuesa, and S. Le Clainche, "Soft Computing Techniques to Analyze the Turbulent Wake of a Wall-Mounted Square Cylinder," Springer International Publishing, 2020, pp. 577-586.

[46] M. A. Mendez, D. Hess, B. B. Watz, and J. M. Buchlin, "Multiscale proper orthogonal decomposition (mPOD) of TR-PIV data—a case study on stationary and transient cylinder wake flows," *Measurement Science and Technology*, vol. 31, no. 9, p. 094014, 2020, doi: 10.1088/1361-6501/ab82be.

[47] G. Berkooz, P. Holmes, and J. L. Lumley, "The Proper Orthogonal Decomposition in the Analysis of Turbulent Flows," Annual Review of Fluid Mechanics, vol. 25, no. 1, pp. 539-575, 1993, doi: 10.1146/annurev.fl.25.010193.002543.

[48] P. Holmes, J. L. Lumley, G. Berkooz, and C. W. Rowley, *Turbulence, Coherent Structures, Dynamical Systems and Symmetry*. Cambridge University Press, 2012, https://doi.org/10.1017/CBO9780511919701.

[49] P. Stoica and R. L. Moses, *Spectral Analysis of Signals*. Upper Saddle River, N.J.: Pearson/Prentice Hall (in Eng.), 2005,

[50] A. Sohankar, A. R. Bahmani, and M. R. Rastan, "An LES study of the wake flow dynamics and heat transfer characteristics of two side-by-side finite wall-mounted square cylinders," *Ocean Engineering*, vol. 266, p. 113104, 2022/12/15/ 2022, doi: https://doi.org/10.1016/j.oceaneng.2022.113104.

[51] M. Y. Younis, M. M. Alam, and Y. Zhou, "Flow around two non-parallel tandem cylinders," *Physics of Fluids,* vol. 28, no. 12, p. 125106, 2016, doi: 10.1063/1.4972549.

[52] S. S. Lu and W. W. Willmarth, "Measurements of the structure of the Reynolds stress in a turbulent boundary layer," *Journal of Fluid Mechanics,* vol. 60, no. 03, p. 481, 1973-09-01 1973, doi: 10.1017/s0022112073000315.

[53] W. K. George, "Lectures in Turbulence for the 21st Century," *Chalmers University of Technology,* vol. 550, 2013.

Appendix A

In this section, the supplementary findings at off-symmetry plane $z/h = 0.1$ are presented. These results exhibit a high similarity with the preceding discussion at the symmetry plane $z/h = 0$. Given the stochastic nature of the pore distribution, distinct spatial modes in **Figure A1** show varying structures. However, by analyzing the modes, we can see that there are time-dependent momentum exchanges caused by turbulent fluctuations in different modes.

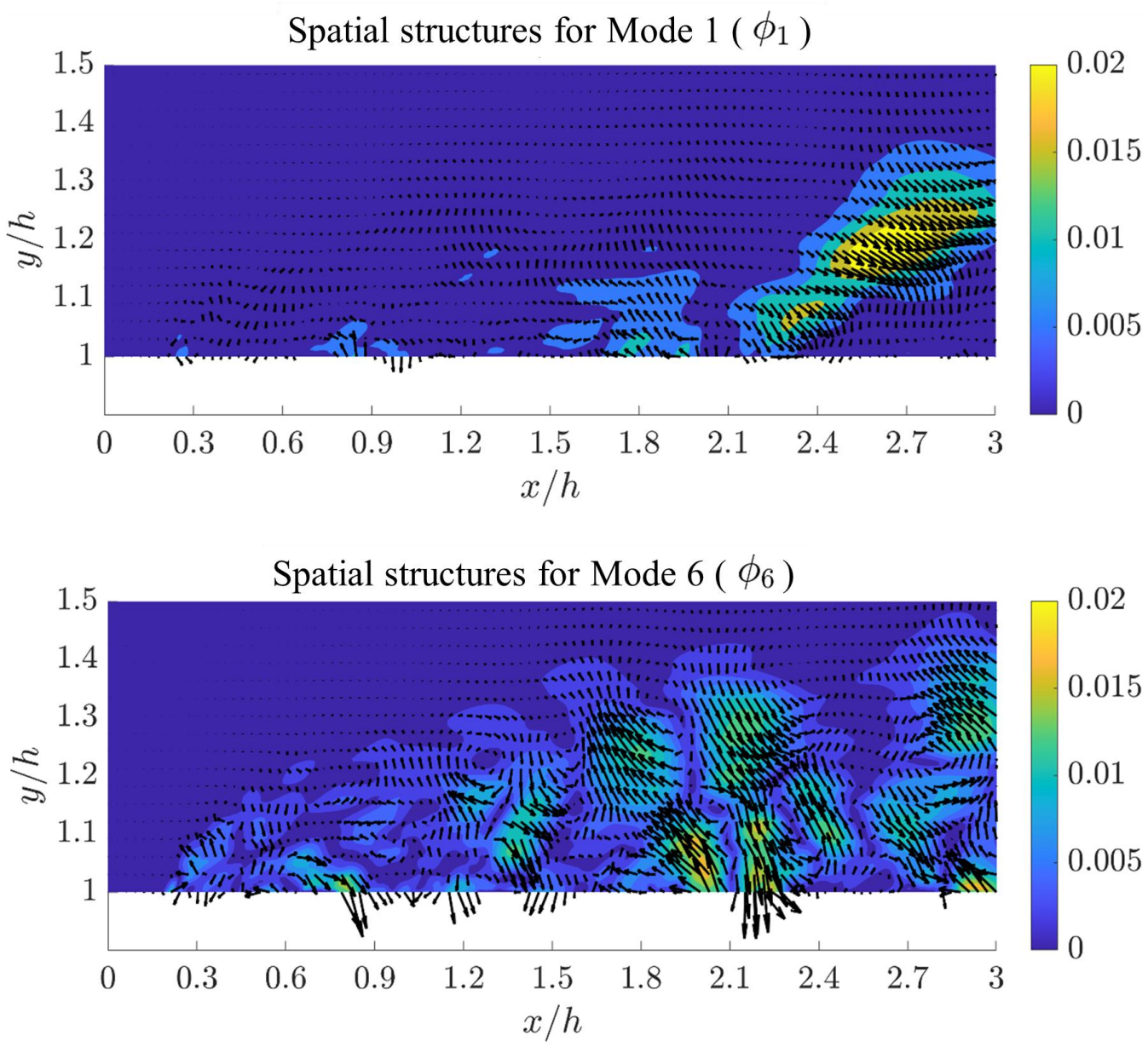

Figure A1. Vector representation of streamwise and vertical velocity component of modes 1 and 6 in the ShearPOD zone at off symmetry plane $z/h = 0.1$; **Top**: Mode 1; **bottom**: Mode 6.

The $\hat{\psi}^r(f)$ of the modes in **Figure A2** show distinct peaks at different Strouhal numbers ($St = fh/U_{in}$ where "f" is frequency). **Table A1** complements these observations by presenting the dominant Strouhal numbers for the initial 20 modes within both the ShearPOD and POD01 zones at off-symmetry plane z/h = 0.1. For example, for the ShearPOD zone, the St in the first row and column shows that for the first mode, the first dominant Strouhal number is St_1^1 = 0.41 where the subscript shows the index of mode, and the superscript shows the index of dominant frequency. For the POD01 zone, St_1^1 = 0.1.

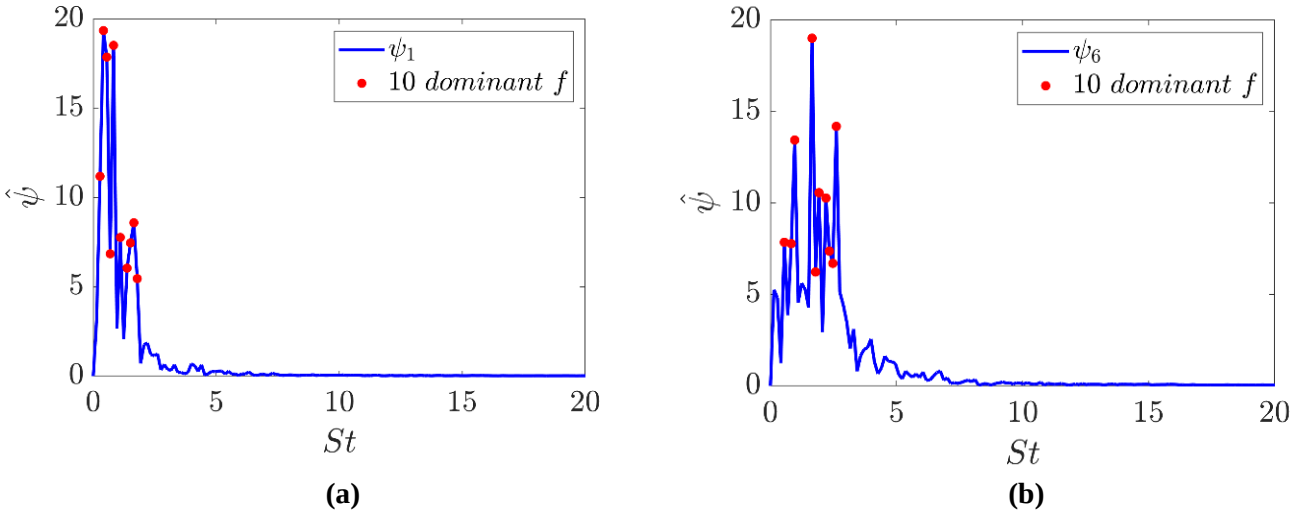

Figure A2. Spectra of temporal modes 1 and 6 in the ShearPOD zone at off-symmetry plane z/h = 0.1. **(a)** Mode 1 at ShearPOD zone; **(b)** Mode 6 at ShearPOD zone.

In **Figure A3**, the co-occurrence of dominant frequencies in the first mode is depicted across two POD zones, namely POD01 and ShearPOD at off-symmetry plane z/h = 0.1. **Figure A3**(**a**) highlights the interaction between the dominant frequencies of mode 1 in the POD01 zone with all 20 initial modes in the ShearPOD zone. The non-zero elements in these figures signify instances where one of the 10 dominant frequencies in mode 1 of the POD01 zone is observed in the ShearPOD zone. For instance, **Figure A3**(**a**) demonstrates that St_2^3 = 1.24, in mode 2 of the ShearPOD zone interact with the 10 dominant frequencies of mode 1 in the POD01 zone. Similarly, it shows the interactions between St_5^1 = 1.65 of ShearPOD zone with the 10 dominant frequencies of mode 1 in the POD02 zone.

Figure A3(**b**) further illustrates the total co-occurrence of all the initial 20 modes in the POD01 zone with all 20 initial modes in the ShearPOD zone. For example, **Figure A3**(**b**) indicates that St_1^6 = 2.06 in the POD01 zone is observed 3 times in all the modes of the ShearPOD zone. Another instance is St_3^5 = 1.24 in **Figure A3**(**b**), signifying that the 5th dominant frequency in mode 2 of the POD01 zone is observed 7 times

841 in all modes of the ShearPOD zone.

Table A1. The first 10 dominant St ($St = fh/U_{in}$ where "f" is frequency) among the initial 20 modes at off-symmetry plane z/h = 0.1.

		Index of dominant St in the POD01 zone									
		1	**2**	**3**	**4**	**5**	**6**	**7**	**8**	**9**	**10**
Index of mode	**1**	0.1	0.31	2.68	1.85	2.88	2.06	2.16	1.24	3.3	3.09
	2	2.16	0.21	2.06	1.75	0.41	1.24	0.82	0.93	2.88	0.51
	3	0.1	2.27	1.34	2.16	1.24	1.75	2.78	2.47	1.85	2.68
	4	0.72	1.34	0.31	0.62	2.47	1.13	0.1	1.65	0.51	0.93
	5	0.82	0.51	1.34	0.31	1.13	1.65	2.16	2.47	0.21	0.93
	6	0.1	1.13	1.44	2.27	2.16	0.72	1.85	0.82	2.06	1.34
	7	0.41	0.31	2.47	0.21	1.54	2.57	1.03	0.51	2.27	2.88
	8	0.72	2.16	1.65	0.93	0.21	0.31	0.41	2.47	0.1	1.75
	9	0.82	1.24	1.75	0.72	0.31	1.54	2.47	2.06	1.96	2.27
	10	0.21	0.93	1.44	2.68	2.16	1.96	0.72	0.1	0.82	3.19
	11	0.51	1.34	0.93	0.62	0.1	0.72	2.16	2.47	1.44	0.21
	12	1.03	0.41	0.31	0.93	0.51	2.57	2.88	0.21	0.62	2.06
	13	2.37	3.3	2.47	0.41	1.85	1.65	1.44	0.31	2.16	0.21
	14	0.41	2.47	1.96	0.1	0.31	1.85	2.16	1.34	0.72	0.82
	15	2.16	1.44	0.82	0.1	1.03	0.51	1.13	1.34	2.57	0.93
	16	2.16	0.72	2.47	1.65	1.24	1.96	1.03	2.37	2.57	0.51
	17	1.65	1.54	2.27	0.82	1.44	1.96	0.41	3.4	1.03	4.02
	18	1.44	0.1	1.03	1.75	0.21	2.78	0.51	0.72	0.31	0.41
	19	1.13	3.19	2.99	0.51	2.16	0.41	5.05	2.57	2.78	0.82
	20	0.62	0.51	0.72	0.1	1.24	1.65	1.34	1.03	2.88	0.31

		Index of dominant St in the ShearPOD zone									
		1	**2**	**3**	**4**	**5**	**6**	**7**	**8**	**9**	**10**
Index of mode	**1**	0.41	0.83	0.55	0.28	1.65	1.1	1.51	0.69	1.38	1.79
	2	1.51	1.65	1.24	0.83	1.1	0.55	1.38	1.79	0.69	0.41
	3	0.41	1.51	0.83	0.28	0.55	1.24	1.1	1.65	1.93	0.69
	4	1.51	0.55	0.41	1.24	0.28	1.93	2.61	0.96	0.69	0.83
	5	1.24	0.69	0.96	0.83	0.28	0.41	2.2	1.51	1.1	1.65
	6	1.65	2.61	0.96	1.93	2.2	0.55	0.83	2.34	2.48	1.79
	7	1.65	2.61	2.2	1.93	2.34	2.48	0.28	1.24	0.41	0.83
	8	1.24	0.96	1.93	1.38	0.41	1.1	1.65	2.06	1.51	3.3
	9	2.61	0.96	1.38	3.3	1.1	2.75	3.03	2.34	0.14	1.79
	10	0.14	0.28	2.06	0.96	0.69	0.41	1.65	1.1	0.55	2.61
	11	0.96	2.2	1.79	2.61	1.65	1.1	2.48	0.14	1.38	3.3
	12	0.96	0.83	2.2	0.28	1.38	2.61	1.65	0.41	0.14	3.16
	13	2.2	0.14	2.75	1.38	3.03	3.16	1.79	0.28	2.48	0.96
	14	1.79	2.61	3.03	0.14	1.38	0.96	1.24	0.28	2.75	2.2
	15	2.61	1.79	3.03	0.55	0.69	2.48	2.89	2.06	3.3	0.96
	16	5.78	5.5	7.01	6.46	6.19	6.6	7.15	6.05	5.09	6.74
	17	2.61	7.01	5.78	6.46	6.19	6.6	5.5	7.15	6.74	7.56
	18	1.79	0.41	1.1	0.69	0.28	1.38	2.2	0.96	5.09	5.5
	19	3.58	1.79	2.75	1.93	3.03	4.13	4.26	3.16	1.51	3.85
	20	1.93	2.89	2.34	1.65	2.2	1.51	1.79	3.3	1.1	0.69

In summary, **Figure A3** shows the interactive dynamics between modes in the porous and non-porous regions at off-symmetry plane $z/h = 0.1$ that supports previous discussions related to the symmetry plane $z/h = 0$ in section 3.4.

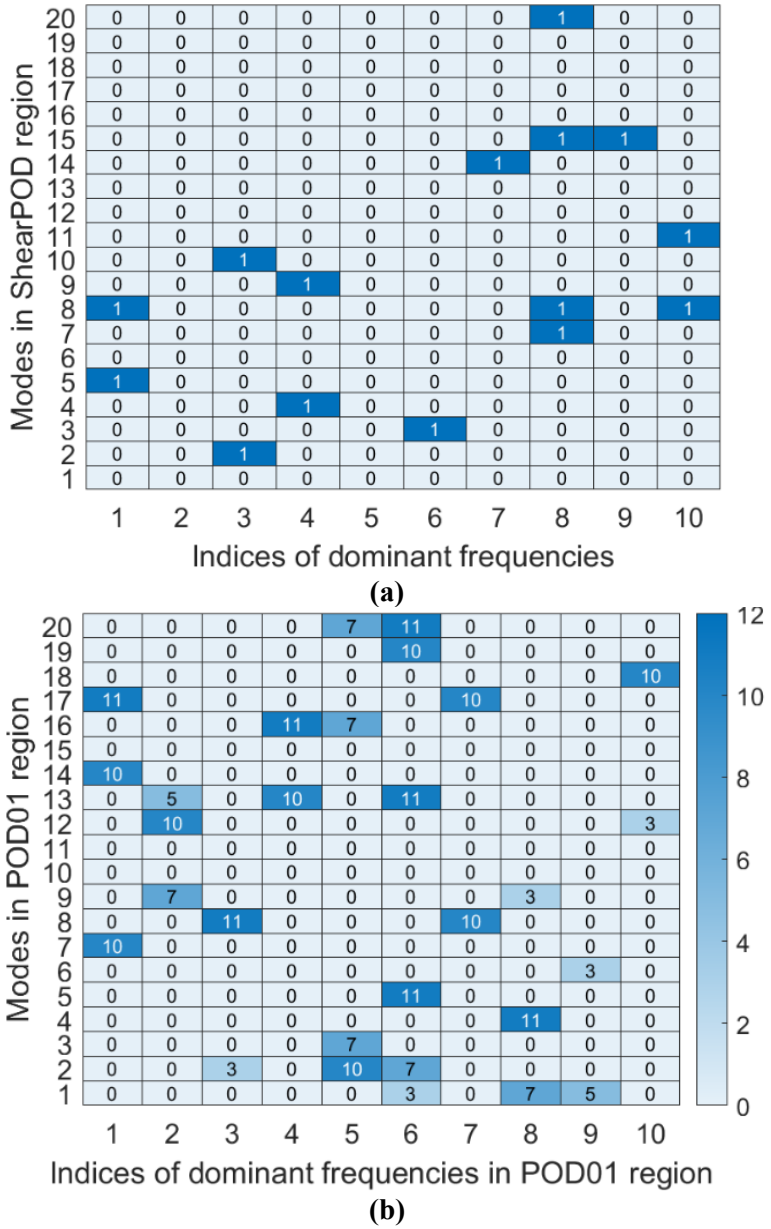

Figure A3. Heatmap of dominate frequencies interaction in POD0 zone inside the porous region with the 20 initial modes in ShearPOD zone in the non-porous region; **Top**: Dominate frequencies interaction between mode1 of POD01 zone and 20 initial modes in ShearPOD zone; **Bottom**: Dominate frequencies interaction between 20 initial modes of POD01 zone and the 20 initial modes in ShearPOD zone; Non-zero values shows the presence of dominate frequencies interaction and zero values shows no interaction between the modes at off-symmetry plane $z/h = 0.1$.